UNIVERSIDAD NACIONAL AUTÓNOMA DE MÉXICO

PROGRAMA DE POSGRADO EN ASTROFÍSICA

INSTITUTO DE ASTRONOMÍA

Estudio de la Formación de Nebulosas Planetarias Bipolares con Núcleos Estelares Binarios.

TESIS

PARA OPTAR POR EL GRADO DE:

DOCTOR EN CIENCIAS (ASTROFÍSICA)

PRESENTA:

Luis Carlos Bermúdez Bustamante

ASESORES:

Dr. Guillermo García Segura, Instituto de Astronomía - UNAM
Dr. Wolfgang Steffen Burg, Instituto de Astronomía - UNAM

Ensenada, B. C., Noviembre 2020.

ACKNOWLEDGMENTS

I thank J. A. Esquivel and J. C. Toledo for making their numerical hydrodynamics code WALICXE3D available. This work is supported by CONACyT grant 51217, 178253 and DGAPA-PAPIIT 104017. *Software credit*: VISIT (Childs et al., 2012).

ABSTRACT

Planetary Nebulae (PNe) are shells of ionized gas surrounding stars with very high effective temperatures. PNe are formed by the hydrodynamic interaction of the ejected envelopes from late-type giant stars with the fast winds and ionizing radiation originating from the remnant stars. The morphology of PNe includes from round and elliptical to bipolar, multipolar and point-symmetric shapes. The causes of this diversity in nebular shapes is one of the most important open questions in the theory of PNe formation and evolution. However, it is thought that the geometry and kinematics of the ejected envelopes (i.e. the distribution of density and velocity in the ejected gas) may trigger the variety of nebular shapes. It is also thought that the majority of bipolar PNe are formed in binary stellar systems. With that in mind, numerical simulations are performed to investigate the stellar wind from interacting binary stars. The aim is to find analytical formulae describing the outflow structure. In each binary system the more massive star is in the asymptotic giant branch (AGB) and its wind is driven by a combination of pulsations in the stellar surface layers and radiation pressure on dust, while the less massive star is in the main sequence. Time averages of density and outflow velocity of the stellar wind are calculated and plotted as profiles against distance from the centre of mass and colatitude angle. It is found that mass is lost mainly through the outer Lagrangian point L_2. The resultant outflow develops into a spiral at low distances from the binary. The outflowing spiral is quickly smoothed out by shocks and becomes an excretion disc at larger distances. This leads to the formation of an outflow structure with an equatorial density excess, which is greater in binaries with smaller orbital separation. The pole-to-equator density ratio reaches a maximum value of $\sim 10^5$ at Roche lobe overflow state. It is also found that the gas stream leaving L_2 does not form a circumbinary ring for stellar mass ratios above 0.78, when radiation pressure on dust is taken into account. Analytical formulae are obtained by curve fitting the two-dimensional, azimuthally averaged density and outflow velocity profiles. The formulae can be used in future studies to set-up the initial outflow structure in hydrodynamic simulations of common-envelope evolution and formation of planetary nebulae.

RESUMEN

Las nebulosas planetarias (NPs) son cascarones de gas ionizado que rodean estrellas con temperaturas efectivas muy altas. Las NPs se forman por la interacción hidrodinámica de las envolventes expulsadas de estrellas gigantes de tipo tardío con los vientos rápidos y la radiación ionizante que se origina de las estrellas remanentes. La morfología de las NPs incluye desde formas redondas y elípticas hasta bipolares, multipolares y con simetría de punto. Las causas de esta diversidad en formas nebulares es una de las preguntas abiertas más importantes en la teoría de la formación y evolución de NPs. Sin embargo, se piensa que la geometría y la cinemática de las envolventes eyectadas (es decir, la distribución de densidad y velocidad en el gas eyectado) puede provocar la variedad de formas nebulares. Se cree también que la mayoría de NPs bipolares se forman en sistemas estelares binarios. Con eso en mente, se realizan simulaciones numéricas para investigar el viento estelar de estrellas binarias interactuantes. El objetivo es encontrar fórmulas analíticas que describan la estructura del flujo. En cada sistema binario la estrella más masiva está en la rama gigante asintótica y su viento es impulsado por una combinación de pulsaciones en las capas superficiales estelares y presión de radiación en polvo, mientras la estrella menos masiva está en la secuencia principal. Promedios temporales de densidad y velocidad del viento estelar son calculados y graficados como perfiles contra la distancia desde el centro de masa y el ángulo de colatitud. Se encuentra que se pierde masa principalmente a través del punto externo de Lagrange L_2. El flujo resultante se transforma en una espiral a distancias cortas desde la binaria. El flujo en espiral es suavizado rápidamente por choques y se vuelve un disco de excreción a grandes distancias. Esto lleva a la formación de una estructura en el flujo con un exceso de densidad ecuatorial, el cual es mayor en binarias con separación orbital menor. La razón de densidad polo a ecuador alcanza un valor máximo de $\sim 10^5$ en el estado de desborbe del lóbulo de Roche. También se encuentra que la corriente de gas que deja L_2 no forma un anillo circumbinario para razones de masa estelar mayores a 0.78, cuando la presión de radiación en polvo se toma en cuenta. Se obtienen fórmulas analíticas por ajuste de curvas a los perfiles bidimensionales y promediados azimutalmente de densidad y velocidad. Las fórmulas se pueden usar en estudios futuros para establecer la estructura del flujo inicial en simulaciones hidrodinámicas de evolución de envolvente común y de formación de nebulosas planetarias.

TABLE OF CONTENTS

LIST OF TABLES

LIST OF FIGURES

Dedication

To my brother Alvaro Javier,
whose calm attitude have taught me
what is really important in life.
Para mi hermano Alvaro Javier,
cuya actitud relajada me ha enseñado
lo que es realmente importante en la vida.

Chapter One

Introduction

After helium core fusion has ceased, single, low- to intermediate-mass stars evolve to a low effective temperature, high surface luminosity region in the Hertzsprung–Russell (HR) diagram known as the asymptotic giant branch (AGB). Stars in the AGB have an electron-degenerate carbon-oxygen core, surrounded from the inside out by a helium-burning shell, a helium-rich inter-shell region, a hydrogen-burning shell and a hydrogen- and helium-rich convective envelope (Habing and Olofsson, 2004).

Observations of molecular emission lines from AGB stars show that many of them undergo mass loss at high rates through slow, dense winds (De Beck et al., 2010; Wittkowski et al., 2018). It is well known that the asymptotic outflow speed of AGB winds is lower than the stellar surface escape velocity (Ramstedt, Schöier, and Olofsson, 2009), in comparison with less evolved Red Giant Branch (RGB) stars (e.g. Carpenter et al., 2018). The above indicates that work is done by the mass-loss mechanism mostly to overcome the gravitational well of the stars, instead of accelerating the winds to their asymptotic speeds. Because of this, most of the wind driving energy should be injected in the inner regions of the flow, since the gravitational potential is inversely proportional to the distance from the centre of the stars. Furthermore, the driving energy must be added as work done by a force rather than as heat, given that radiative cooling is very efficient in the inner parts of the dense winds (Holzer and MacGregor, 1985; Lamers and Cassinelli, 1999).

Mass-loss rates in AGB stars increase with pulsation period, bolometric luminosity and optical depth at infrared wavelengths (Wood, 2000; Sloan et al., 2010; Danilovich et al., 2015; McDonald et al., 2018). From these results it is thought that AGB winds are driven by a combination of pulsation-induced shockwaves and radiation pressure on dust (Nowotny, Höfner, and Aringer, 2010). The shockwaves eject material into the stellar atmosphere to distances where dust is formed under low temperature and high density conditions. The dust is then accelerated by absorption and scattering

of the stellar radiation field and transfers its momentum to the gas through collisions, inducing a slow wind (Höfner and Olofsson, 2018). This is basically the scenario that we include in this study. Nevertheless, it should be said that a complete explanation, based on first principles, of the mass-loss mechanism for late-type giant stars is still missing, as exemplified by the following issue: The timescale in which AGB stars shed their envelopes is of $\sim 10^3$ yr only (Miller Bertolami, 2016), thus the rate of mass loss can be as high as $\sim 10^{-3}\ M_{\odot}/yr$. However pulsation, dust-driven winds in single AGB stars has a maximum mass-loss rate of $\sim 10^{-5}\ M_{\odot}/yr$ (chapter 7 of Lamers and Cassinelli, 1999; Höfner and Olofsson, 2018).

Once the mass of the remnant envelope is reduced to values of $\sim 10^{-2}$ $M_{\odot}$, the slow wind is over and the star begins to move towards higher effective temperatures at nearly constant luminosity in the HR diagram (Miller Bertolami, 2016). When temperatures of $\sim 25,000$ K are reached, radiation from the star ionises the inner parts of the ejected envelope. The ionized gas, hereinafter known as the shell, expands into the still neutral envelope because of the higher thermal pressure of the former. The expansion of the ionization front is supersonic with respect to the neutral gas, therefore it creates a shock (Mellema, 1994). At about the same time a new stellar wind, probably driven by scattering on resonance lines (Pauldrach et al., 1988), is generated. The terminal velocity of a line-driven wind is proportional to the escape velocity from the star (Pauldrach et al., 1988), consequently the new stellar wind becomes faster as the star shrinks while moving towards the blue in the HR diagram. Once the wind speed reaches ~ 150 km s^{-1}, the interaction between the shell and the wind produces two shockwaves: one of them moves downstream and sweeps the inner parts of the shell into a rim, while the other one moves upstream and creates a bubble of hot gas by converting the wind kinetic energy into heat (Kahn and Breitschwerdt, 1990). A Planetary Nebula (PN) consists of the rim + shell system and its inner edge is a contact discontinuity separating the rim from the hot bubble, while its outer edge is the shock front separating the shell from the still undisturbed slow wind. It is worthy to mention that this system is not static, but changes as the speed of the fast wind increases. For example, at early stages the shell is faster than the rim, but the latter accelerates owing to the increasing thermal pressure of the hot bubble. Also, as the star becomes hotter, the ionization front breaks through the PN outer edge and begins to ionise the slow AGB wind (Perinotto et al., 2004).

The model of PN formation described above, which is based on the Interacting Stellar Winds (ISW) model by Kwok, Purton, and Fitzgerald (1978) was applied only to round objects originally.

However, several other shapes are possible as shown in Figure 1.1 and, even more, round PNe only constitute ~ 20 per cent of all observed objects (Manchado, 2004; Parker et al., 2006). The mechanisms causing these shapes, specially the bipolar, are still an unsolved problem, but it is thought that they operate at the tip of the AGB phase or at the early post-AGB phase (Balick, 1987; Corradi and Schwarz, 1995; Manchado et al., 1996; Sahai et al., 2007), as shown in Figure 1.2.

Some numerical computations, in the context of the ISM model (Kwok, 2002), have reproduced diverse nebular shapes on the assumption of various functions for the density and outflow velocity distribution in the slow AGB wind (Mellema, Eulderink, and Icke, 1991; Icke, Balick, and Frank, 1992). For example, bipolar PNe can be formed if the slow wind density increases continually from the poles to the equator (Kahn and West, 1985; Balick, 1987; Icke, Preston, and Balick, 1989; Soker and Livio, 1989; Dwarkadas, Chevalier, and Blondin, 1996; García-Segura, Langer, et al., 1999; Huarte-Espinosa et al., 2012). Several mechanisms to generate the required equator-to-pole density ratio have been suggested in the literature, such as stellar rotation, magnetic fields, surviving protostellar discs, accretion-powered jets and the gravitational field of a companion star.

Deviations of isotropic mass-loss by centrifugal forces in a rotating AGB star are discussed by Asida and Tuchman (1995). Their model is based on numerical results by Bowen (1988), in which the AGB stellar atmosphere is levitated by pulsation-induced shocks to distances of up to ~ 10 stellar radii. For a rotating AGB star, the centrifugal force in this levitated atmosphere is a significant fraction of the gravitational force at the equatorial plane, where mass-loss can be higher compared to the stellar poles. However, for this mechanism to be effective, the AGB star should have rotated much faster than its critical rate while it was on the main sequence (assuming rigid body rotation and conservation of angular momentum as the star evolves) (García-Segura, Villaver, Langer, et al., 2014). In other words, the progenitor AGB star requires an external source of angular momentum to shape a bipolar PN.

Magnetic fields in rotating AGB stars have an azimuthal component, which decreases with magnitude as the inverse of the distance from the stellar surfaces (in other words, it follows a r^{-1} power-law) (Chevalier and Luo, 1994). At large distance the azimuthal (or toroidal) magnetic pressure is higher than the thermal pressure of AGB winds. Because of that, even if slow winds are spherically symmetric, the shocked fast winds will advance along the poles, where magnetic fields are weaker. A natural consequence is the formation of bipolar PNe. However, a significant problem in this model

Figure 1.1 Morphology diversity of Planetary nebulae: **Top to bottom, left to right:** Round IC 3568. Elliptical NGC 2022. Bipolar Hen 2-437. Multi-polar NGC 2440. Point-symmetric NGC 6543. Irregular NGC 5189. **Credits:** IC 3568 and Hen 2-437: ESA/Hubble & NASA, Acknowledgement: Judy Schmidt. NGC 2022: ESA/Hubble & NASA, R. Wade. NGC 2440: NASA, ESA, and K. Noll (STScI). NGC 6543: ESA, NASA, HEIC and The Hubble Heritage Team (STScI/AURA). NGC 5189: NASA, ESA and the Hubble Heritage Team (STScI/AURA).

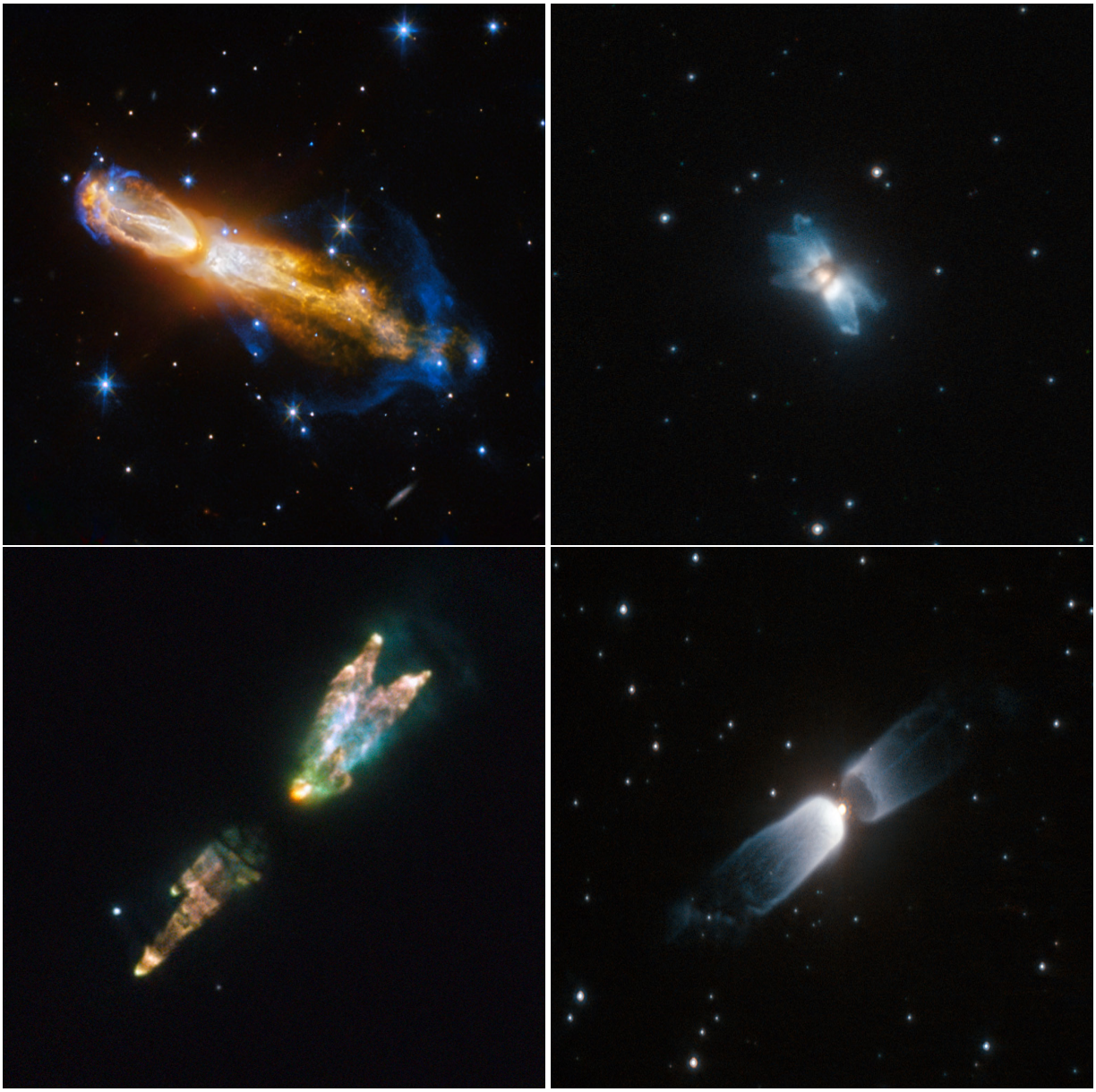

Figure 1.2 Four proto-Planetary Nebulae (PPNe) which show morphologies quite different from spherical. **Top to bottom, left to right:** OH 231.84 + 4.22 (also known as the Calabash Nebula). IRAS 19024+0044. CRL 618 (also known as the Westbrook Nebula). IRAS 13208-6020. **Credits:** OH 231.84 +4.22: ESA/Hubble & NASA, Acknowledgement: Judy Schmidt. IRAS 19024+0044: ESA/Hublle, NASA and R. Sahai. CRL 618 and IRAS 13208-6020: ESA/Hubble & NASA.

is the sustainment of such magnetic fields during all the time the AGB stars produces stellar winds (Nordhaus, Blackman, and Frank, 2007). Dynamo generation of magnetic fields drains the angular momentum of the AGB stars in such a short timescale that magnetic fields becomes irrelevant to the outflow dynamics before the onset of fast winds (Blackman, 2004). Again, one sees that magnetic fields (the shaping mechanism) require an external source of angular momentum to produce bipolar PNe.

The AGB slow wind can be deviated from the spherical morphology by the presence of a surviving protostellar disc, as suggested by Livio (1995) and by Kastner and Weintraub (1995) for the proto-PN OH 231.84 + 4.22 (The Calabash Nebula). In this model the disc is replenished in mass through a stellar wind during the RGB phase. Thus the disc becomes dense enough to stop the AGB slow wind and to divert it along the poles. Disadvantages of this mechanism include: (i) The gas forming protoplanetary discs needs a source of angular momentum that a single AGB star cannot supply (Bujarrabal et al., 2013); (ii) Bipolar PNe have more massive progenitor stars, as deduce from observations (Corradi and Schwarz, 1995; Stanghellini et al., 2006), however protoplanetary discs dissipate faster, through the action of viscous dissipation and photoevaporation, around high-mass stars than around solar-type stars (Williams and Cieza, 2011); (iii) Mass loss occurs preferentially along the poles, which is the contrary of what it is expected for the formation of bipolar PNe and (iv) A protostellar disc does not explain the fast outflows observed in the Calabash Nebula.

Bipolar PNe can be shaped by collimated fast winds (jets) which advance through the circumstellar envelope along two opposite directions, creating high-temperature, low-density bubbles of shocked material that inflate the two lobes (Soker, 2002). On the one hand, observations indicate that the momentum of these jets is too high to be powered by the stellar radiation flux (Alcolea et al., 2001). On the other hand, accretion discs (produced by binary stars) may provide the momentum required by the jet, although theoretical models of jet generation by accretion discs are not conclusive yet (Hernández et al., 2014). In any case, it is difficult to explain how single AGB stars develop high-velocity bipolar outflows.

In view of the foregoing, the gravitational field of a companion star is the most promising (i) cause of anisotropic mass loss in AGB stars, (ii) shaping mechanism in PNe (García-Segura, Villaver, Langer, et al., 2014). In fact, only a minority of symbiotic stars are surrounded by spherical nebulae (Corradi, Brandi, et al., 1999), while up to ~ 40 per cent of the symbiotic stars are in bipolar nebulae

(Schwarz and Monteiro, 2004). Furthermore, morpho-kinematical models of some PNe show that their symmetry axes are perpendicular to the orbital plane of their binary cores (e.g. Jones et al., 2012). The extremely low probability for this perpendicularity to be a random event (Hillwig et al., 2016), indicates a physical link between binary stars and nebular morphology. In Figure 1.3 are shown some bipolar PNe with confirmed binary nuclei.

Approximately 58 per cent of F- and G-type Population I stars belong to binary or multiple systems (Fuhrmann et al., 2017). The orbital separation in some of the binary systems is short enough to allow the interaction between their component stars through tides and/or mass transfer at some point in the binary evolution. Systems of this type are known as interacting binary stars and they are studied in the context of the Roche model (Kopal, 1959), where it is assumed that the stars (i) are point sources of gravity, (ii) follow circular orbits around their common centre of mass (barycentre),(iii) rotate about axes perpendicular to the orbital plane with a period of rotation equal to the orbital period. Under these assumptions there is a rotating frame of reference in which both stars are static and the equipotential surfaces of the system are defined by gravity and centrifugal forces only. The curves ξ_1, ξ_2 and ξ_3 shown in the Figure 1.4 are the intersections of the equipotential surfaces with the orbital plane.

The lemniscate curve ξ_1 passing through the internal Lagrangian point L_1 of the binary system is associated with two closed equipotential surfaces, which define two volumes known as the Roche lobes, with a star inside each one of them. The importance of the Roche lobes for binary stellar evolution is that interacting binaries can be classified according to whether or not the stars fill these lobes (Kopal, 1959). For instance, in detached binaries none of the two stars fill their Roche lobes and the wind from the donor star is focused towards the internal Lagrangian point L_1 by the gravitational field of the receiver star. If the wind has a high specific angular momentum an accretion disc around the receiver star is created, on the contrary the wind hits the receiver star surface. In semi-detached binaries, one of the stars (the donor) fills its lobe, as a consequence material directly from the stellar surface flows through the internal Lagrangian point L_1 to the receiver star. Again, an accretion disc will form if the gas flow has a high angular momentum. Finally, in contact binaries both stars fill their Roche lobes and share a common envelope (CE). As a consequence, the stellar components in a contact binary have similar effective temperature and luminosities, even if the stellar masses are different (Binnendijk, 1965).

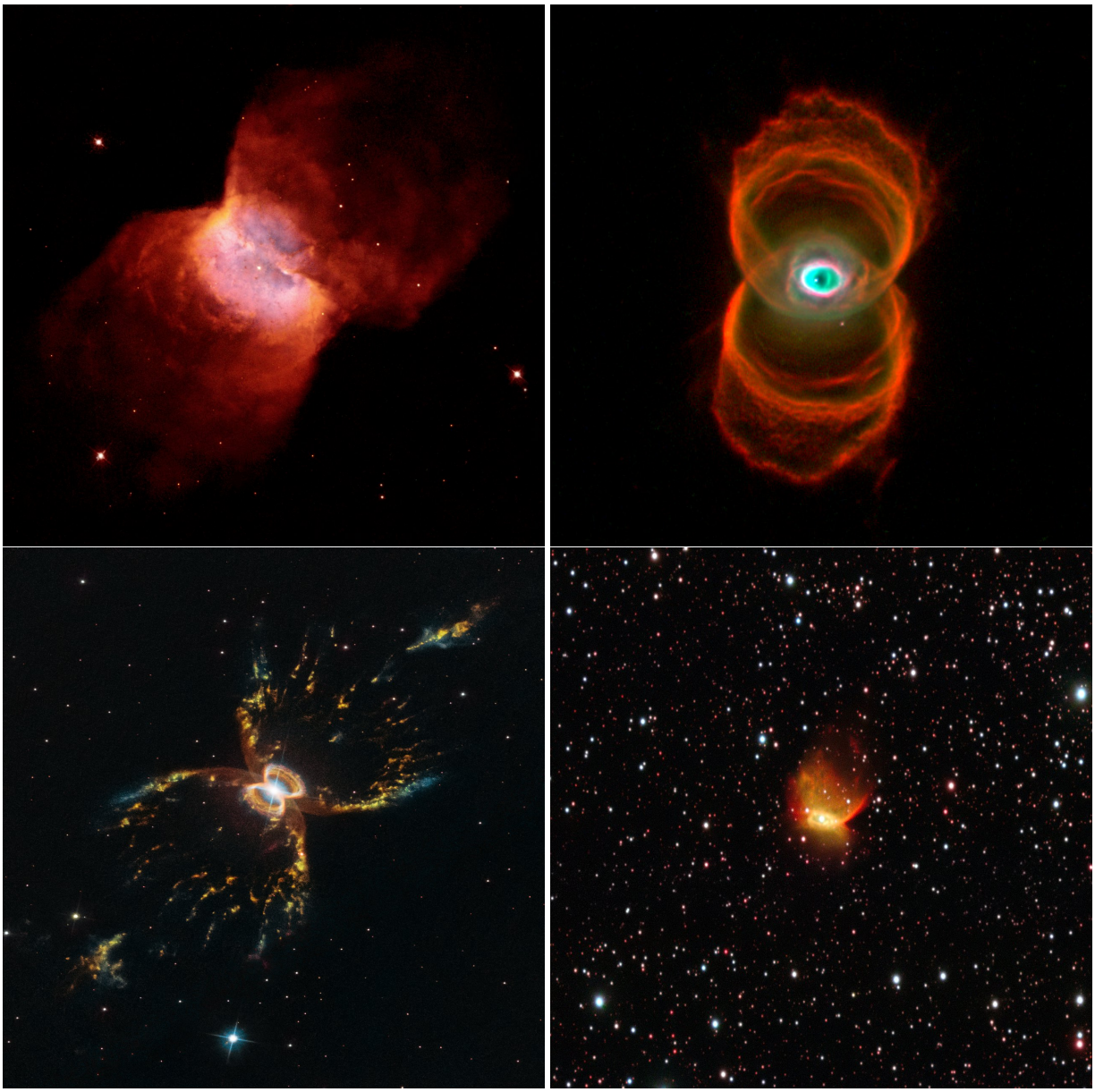

Figure 1.3 Bipolar PNe with binary central stars. **Top to bottom, left to right:** NGC 2346. MyCn 18. Hen 2-104. Hen 2-428. **Credits:** NGC 2346: NASA/ESA and the Hubble Heritage Team (AURA/STScI). MyCn 18: R. Sahai and J. Trauger (JPL), the Wide Field and Planetary Camera 2 team and NASA/ESA. Hen 2-104: NASA, ESA and STScI. Hen 2-428: ESO.

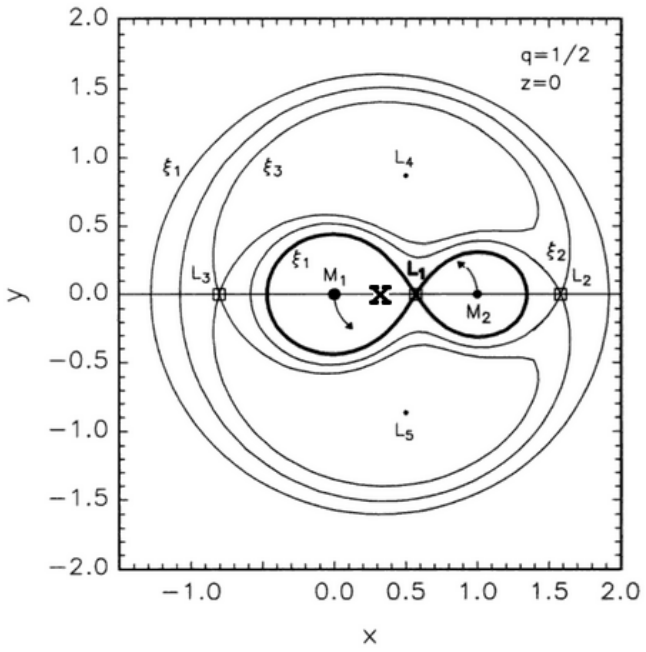

Figure 1.4 Roche equipotential curves for a stellar mass ratio $q = M_2/M_1 = 1/2$ in the orbital plane. Three curves (ξ_1, ξ_2 *and* ξ_3) are labeled. Boxes ($\square$) enclosed three of the Lagrangian points. The $\times$ symbol is the centre of mass of the system. The unit of distance for coordinates *(x,y)* is the orbital separation between the stars. **Credit:** Hansen, Kawaler, and Trimble (2004).

For the case of contact binaries, the maximum volume of their CE is limited by the closed surface whose intersection with the orbital plane is the inner equipotential curve ξ_2. Once the CE swells and reaches this closed surface, matter will start to flowing out through the Lagrangian point L_2. The CE can be kept in co-rotation by the action of dissipative forces throughout several orbital periods. However the gas leaving L_2 is not longer forced to co-rotate, but it can still be gravitationally bound to the binary stars. In that case, the outflowing gas may form a circumbinary ring.

The subject of study of the present thesis are interacting binaries whose primary stars (the more massive ones) are in the AGB and overflow their Roche lobe or are close to do it, while their secondary stars (the less massive ones) are in the main-sequence. This type of stellar systems are of great importance since it is thought that they are responsible for the formation of bipolar PNe. Supporting evidence for this hypothesis are observations of binary central stars in PNe with orbital separations smaller than the typical radius of the progenitor AGB star (De Marco, 2009). For the companion to survive the AGB phase, the initial orbital separation of the system must be much larger. This indicates that a huge amount of mass and angular momentum was lost during the AGB and post-AGB phases.

The more the stars overflow their Roche lobe, the more material is transferred to their companions. For a primary AGB star with a deep convective envelope in a semi-detached binary, its stellar

radius increases and its Roche lobe radius decreases as consequences of mass loss (Paczyński, 1965; Pavlovskii and Ivanova, 2015). In that case, the process of mass transfer is unstable (although its details are not completely understood yet). A close binary can be formed if the main-sequence secondary star cannot accrete or expel rapidly enough the donated material, from which a CE is formed (Ivanova, Justham, Chen, et al., 2013). Gravitational drag transports orbital energy and angular momentum from the stellar system to the CE and reduces the orbital separation. The envelope is ejected leaving a tight binary star if sufficient energy is transferred, otherwise a stellar merger will occur. For binary stars with similar masses, the common envelope ejection could be more violent, either at the RGB phase or at the AGB phase.

Numerical simulations indicate that this process may occur on time scales of the order of 10^3 *yr* (Chamandy, Tu, et al., 2019) and may lead to the complete ejection of the AGB convective envelope if, among other sources of energy, recombination is taken into account (Paczyński and Ziółkowski, 1968; Tuchman, Sack, and Barkat, 1978; Ivanova, Justham, and Podsiadlowski, 2015). Numerical simulations also show that one natural advantage of evolution by common envelope is that mass loss is confined near the orbital plane (Bond and Livio, 1990; Mohamed and Podsiadlowski, 2007). Thus a bipolar nebula may be formed after this ejected envelope interacts with both the fast wind and the ionizing radiation of the hot remnant core. In other words, it is suggested that PNe with binary cores are shaped by the geometry of the common envelope ejection. Unfortunately, aspherical PNe formation by CE evolution is not fully understood (García-Segura, Ricker, and Taam, 2018), given that the details of the ejection mechanisms or their efficiency are unknown (Sabach et al., 2017), and observations of this brief stellar phase are difficult.

A particular prediction from numerical simulations of CE evolution is a spiral outflow (Figure 1.5), which is formed when gas from the external layers of the accretion disc flows through the closest external Lagrangian point L_2. The stream of leaving matter describes a spiral pattern owing to the orbital motion of the binary system. This spiral outflow has a high specific angular momentum, thus if the mass-loss rate through the L_2 is considerably high, the orbital separation of the binary system is reduced as a consequence of the angular momentum loss (Sepinsky et al., 2009). Observations by The Atacama Large Millimeter/submillimeter Array (ALMA) and The Hubble Space Telescope show spirals in the circumstellar envelopes of evolved stars (Figures 1.6 and 1.7), which seem to confirm the presence of companion star.

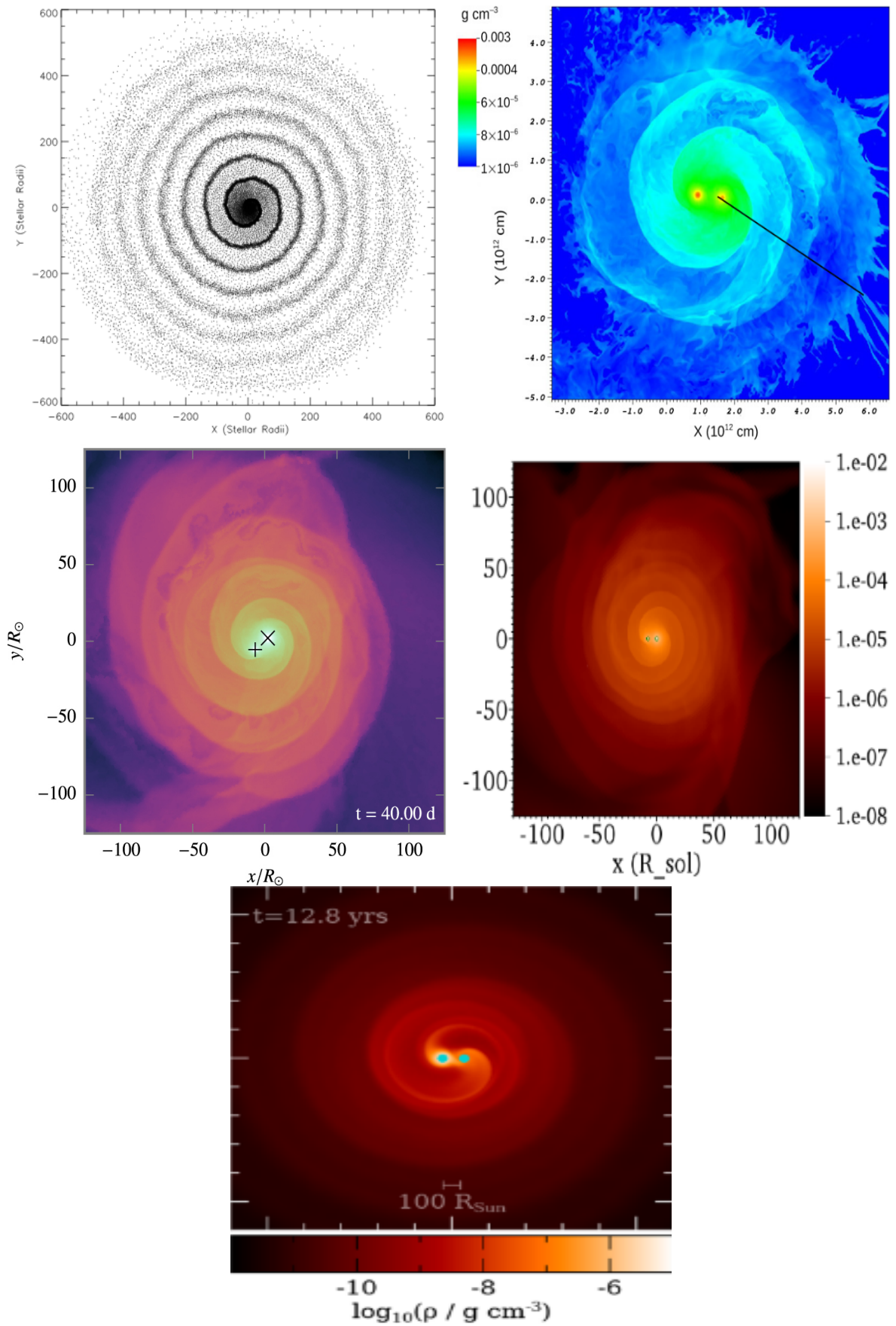

Figure 1.5 Spiral outflows in numerical simulations of CE evolution. The snapshots show the gas density distribution at the orbital plane. **Credits from top to bottom, left to right:** Mastrodemos and Morris (1999), Ricker and Taam (2012), Ohlmann et al. (2016), Chamandy, Frank, et al. (2018), Reichardt et al. (2019)

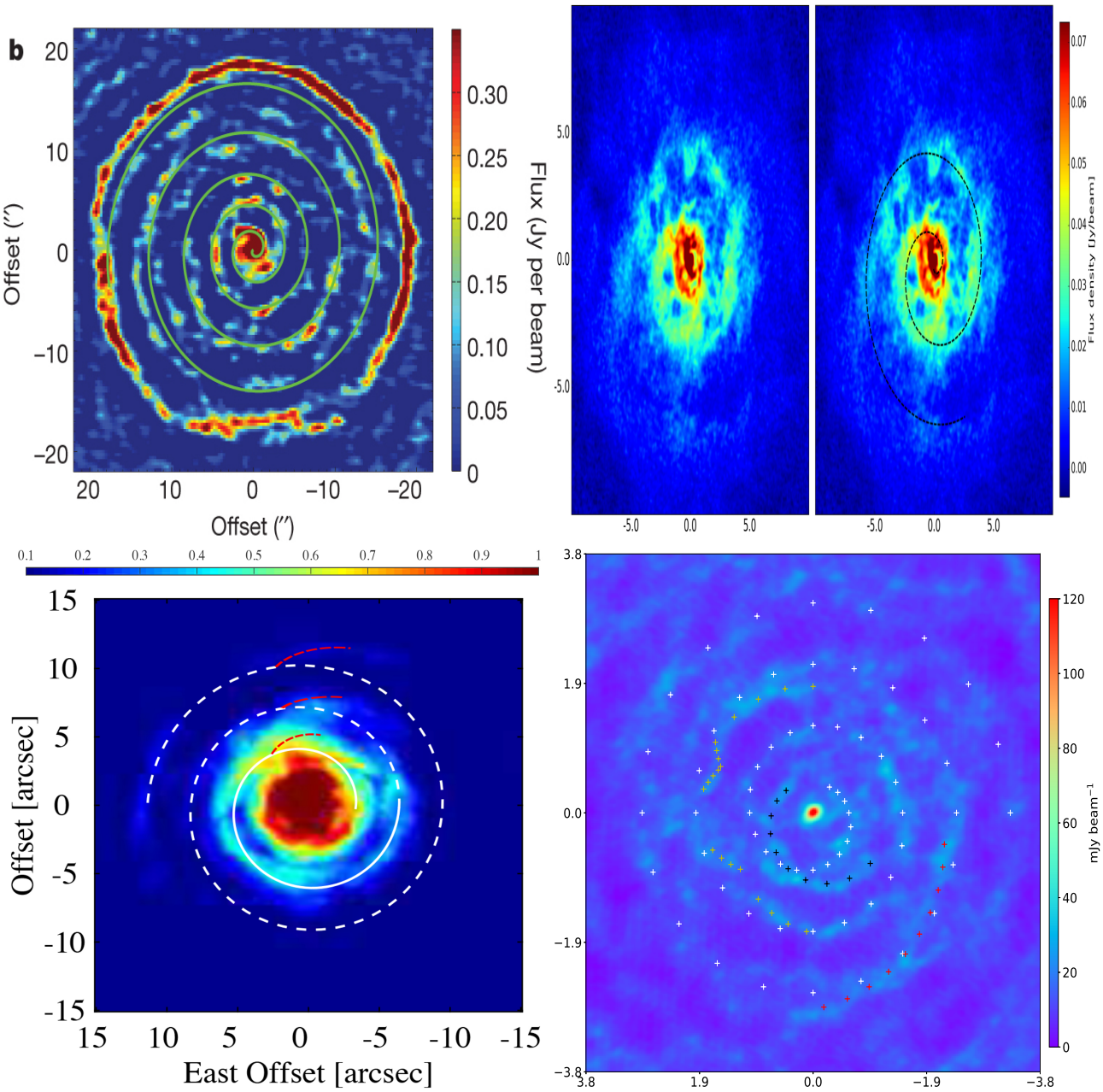

Figure 1.6 *ALMA* observations at the systemic velocity channel of CO line emissions. Colour scales give the flux in Jy per beam. **Top to bottom, left to right:** CO(J=3–2) emission from the AGB star R Sculptoris. The spiral shows linear fits to the emission peaks. Taken from Maercker et al. (2012). CO(v=0, J=2–1) emission from the AGB star EP Aquarii. Taken from Homan et al. (2018). ^{12}CO(J=3–2) emission from the AGB star π^1 Gruis. Taken from Doan et al. (2020). ^{12}CO(J=2–1) emission from the AGB star GX Monocerotis. Taken from Randall et al. (2020).

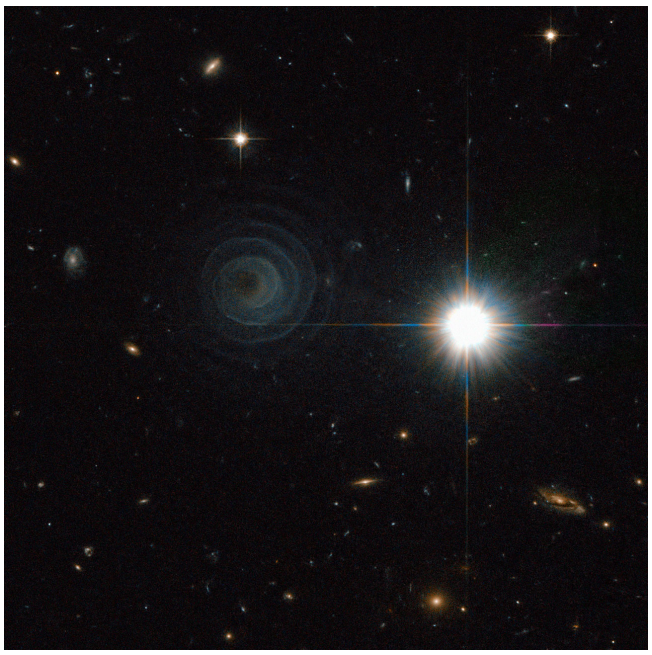

Figure 1.7 Spiral pattern in the envelope of the Mira variable star LL Pegasi. **Credit:** ESA/NASA & R. Sahai

With the current computing power, hydrodynamic simulations of the entire CE phase are not possible, owing to its three-dimensional geometry and the wide range of length and time scales of the physical processes involved (Prust and Chang, 2019). In consequence numerical studies placed an emphasis on the dynamical spiral-in phase (Ricker and Taam, 2012; Passy et al., 2012). However, initial conditions in computations of CE evolution may affect the outcome, specially when the orbital separation shrinks on dynamical timescales, not giving enough time for dissipation of the density structures formed immediately before. Therefore, a constant-density background gas in pressure equilibrium with the surface of the primary star at the onset of simulations (Ricker and Taam, 2012; Staff et al., 2016), or placing the companion star on the surface of the red giant (Ohlmann et al., 2016) may not be realistic situations. In order to improve computations of CE evolution, specially the interaction of the CE ejecta with the previous circumbinary medium, the structure of the gas around the binary system has to be realistically calculated. Thus, the interaction of the AGB wind with the secondary star is very important in this context.

The effects of a stellar companion in the hydrodynamics of the AGB wind were previously investigated by Mastrodemos and Morris (1999), Gawryszczak, Mikołajewska, and Różyczka (2002), Mohamed and Podsiadlowski (2007), and Chen et al. (2017), considering only detached binaries. For the above cases, the AGB wind can be simple, well modelled as a supersonic flow, with a constant expansion velocity of the order of 15 $\mathrm{km\,s^{-1}}$ (Loup et al., 1993). However, for the case of semi-

detached binary stars, the computation of the AGB wind has to be solved from the stellar surface, since the orbit of the binary lies inside the region where the AGB wind is accelerated. Thus, much more physics needs to be included in the modelling, and a more complete knowledge of the AGB wind has to be taken into account. In other words, the form in which the gas is ejected from the stellar surface and is accelerated up to the asymptotic expansion velocity has to be explicitly computed.

We perform numerical simulations of the stellar wind in both detached and semi-detached binary stars. Our goal is to obtain analytical formulae describing the density and outflow velocity of the wind, which can be useful in modelling the interaction of the CE ejecta with the surrounding medium and the later formation of bipolar PNe (García-Segura, Ricker, and Taam, 2018). We focus on the effects of orbital separation and stellar mass ratio on the outflow. To the best of our knowledge, our work is the first attempt to predict the distribution of density and outflow velocity in the stellar wind, based on hydrodynamic models of interacting binaries. In this thesis, 2-dimensional, azimuthally averaged, analytical fits of the outflow structure are obtained. Although our simulations are limited by resolution, the qualitative results give an important first insight of such a complex 3D problem.

The numerical set-up is described in chapter 2. The effects of orbital parameters and stellar mass ratio q on the outflow structure are described in chapter 3. Discussions of results are presented in chapter 4 and conclusions are provided in chapter 5.

Chapter Two

Numerical Method

2.1 The hydrodynamic code

Numerical simulations are performed with the WALICXE3D hydrodynamic code (Toledo-Roy et al., 2014), which is originally designed to run in parallel in a Cartesian adaptive mesh and is a three-dimensional (3D) extension of the WALICXE code (Esquivel et al., 2010).

The computational domain extends $9000 \times 9000 \times 4500\ R_{\odot}$ ($41.76 \times 41.76 \times 20.88$ au) in the X, Y and Z coordinates, respectively and the shortest dimension Z is perpendicular to the orbital plane (XY plane) of the binary system. The original code WALICXE3D is modified through the development of a nested mesh scheme, for the problems studied in this thesis, to concentrate the highest resolution always at the centre of the domain, instead of using the adaptive mesh refinement algorithm. Based on this, the domain is composed of three nested meshes fixed to an inertial frame of reference, whose origin coincides with the centre of mass (barycentre) of the binary system (Figure 2.1). Each mesh has $128 \times 128 \times 64$ cubic cells and is a factor of 2 smaller in each dimension compared to the next coarser mesh. The formal resolution limit in mesh-based codes is set by the Nyquist wavelength, which is the lowest wavelength for a wave to reliably propagate across the grid. The Nyquist wavelength is equal to twice the smallest space interval on the mesh (Bodenheimer et al., 2007). Thus the maximum resolution in our simulations is ~ 35.2 $R_{\odot}$, which corresponds to twice the size of each cell in the innermost mesh (~ 17.6 $R_{\odot}$). We impose a reflective boundary condition at the orbital plane and a free-outflow boundary condition at the other faces of the largest mesh.

WALICXE3D employs a Godunov's second-order upwind method for solving the gas-dynamic equations (also known as the Euler equations) in conservative form:

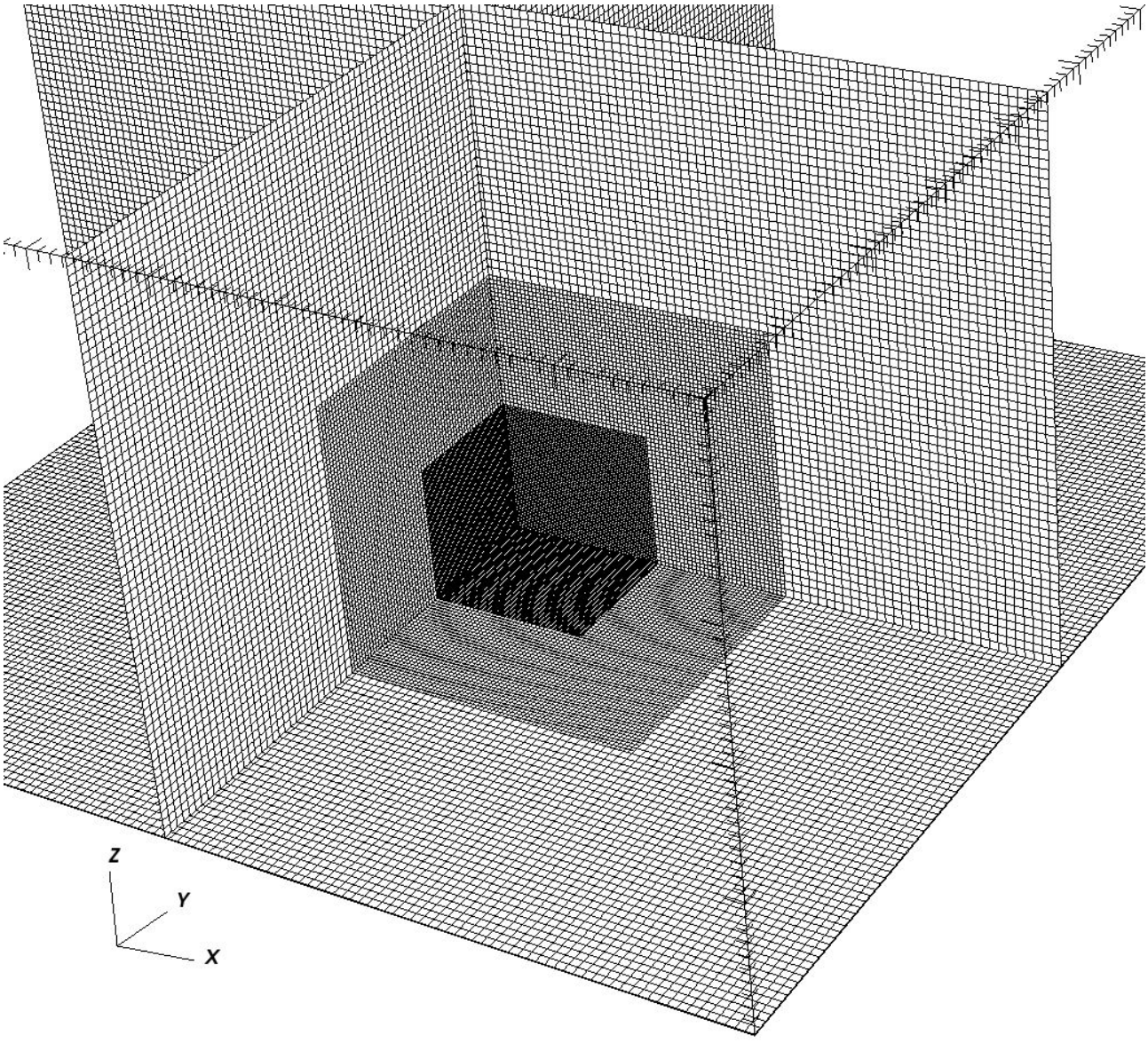

Figure 2.1 Squematic view of the three-dimensional nested meshes.

$$\frac{\partial \mathbf{U}}{\partial t} + \nabla \cdot \mathbf{F}(\mathbf{U}) = -\mathbf{S} \tag{2.1}$$

Where $\mathbf{U} = [\rho,\ \rho\vec{u},\ E]$ is the vector of conserved variables, $\mathbf{F}(\mathbf{U}) = [\rho\vec{u},\ \rho\vec{u}\vec{u} + \mathbb{I}P,\ \vec{u}(E+P)]$ is the vector of fluxes and $\mathbf{S} = [0,\ \rho\nabla\Phi,\ \rho\vec{u}\cdot\nabla\Phi + n\cdot n_e\cdot\Lambda_H(T) + n\cdot n_{CO}\cdot\Lambda_{CO}(T)]$ is the vector of source terms. The symbol $\mathbb{I}$, in the second component of $\mathbf{F}(\mathbf{U})$ is the rank-2 unit tensor. That is, $\mathbb{I}$ is a 3×3 matrix, where each element is equal to 1 inside the main diagonal and zero otherwise. The gas density ρ, the gas velocity field $\vec{u}$ and the gas pressure P are knwon as the hydrodynamic variables. The sum of the internal energy density ε and the kinetic energy density is given by $E = \varepsilon + \frac{1}{2}\rho\,|\vec{u}|^2$. The internal energy density ε is related to the gas pressure by means of the ideal gas equation of state $\varepsilon = \frac{P}{\gamma-1}$, where γ is the ratio of specific heats.

The intercell numerical fluxes $\mathbf{F}(\mathbf{U})$ are computed using the Harten-Lax-van Leer contact (HLLC) approximate Riemann solver (Toro, Spruce, and Speares, 1994; Toro, 2019) and a linear spatial reconstruction of the hydrodynamic variables at the cell faces. Second-order methods develop spurious oscillations where shocks or discontinuities are present (Sweby, 1984). For avoiding this, WALICXE3D uses an averaging function to limit the gradient of the hydrodynamic variables ρ, $\vec{u}$ and P near shocks or discontinuities.

The outflow self-gravity is neglected (see discussion), while the gravitational potential Φ of the binary system is obtained approximating the stars as point sources of gravity (e.g. de Val-Borro, Karovska, and Sasselov, 2009; Chen et al., 2017). The gravitational acceleration in the outflow, caused by the potential Φ, is not computed in the original version of the code WALICXE3D. With that in mind, another modification to the original code is a routine, based on the Störmer-Verlet algorithm (Hairer, Lubich, and Wanner, 2003), to calculate the change of velocity by gravity. As a first step the algorithm calculates the outflow position $\vec{r}$ at time $t+\Delta t$ as follows:

$$\vec{r}(t+\Delta t) = \vec{r}(t) + \vec{v}(t)\cdot\Delta t + 0.5\cdot\vec{g}(t)\cdot(\Delta t)^2 \qquad \text{[au]} \tag{2.2}$$

where $\vec{v}(t)$ is the outflow velocity at time t and $\vec{g}(t)$ is the gravitational acceleration due to the stellar point masses only. In the second step $\vec{g}(t+\Delta t)$ is derived from the gravitational potential of the binary system using the new position $\vec{r}(t+\Delta t)$. In the final step, the outflow velocity is calculated at time $t+\Delta t$ as follows:

$$\vec{v}(t+\Delta t) = \vec{v}(t) + 0.5 \cdot (\vec{g}(t) + \vec{g}(t+\Delta t)) \cdot \Delta t \qquad [\mathrm{km/s}] \quad (2.3)$$

As a remark, this algorithm assumes that the acceleration $\vec{g}(t+\Delta t)$ only depends on position $\vec{r}(t+\Delta t)$ and does not depend on velocity $\vec{v}(t+\Delta t)$. This condition is clearly fulfilled for the problems studied here.

Radiative cooling in the original code WALICXE3D is implemented only at temperatures larger than 10^4 Kelvins. Therefore another modification to the hydrodynamic code is the implementation of a totally different cooling law at temperatures between $\sim 10^3$ and $\sim 10^4$ K, where the contribution of molecules (in this case carbon monoxide (CO)) and collisional excitation of hydrogen by free electrons have to be taken into account. In the dense outflows from AGB stars, the cooling timescale t_{cool} is much lower than the hydrodynamic timescale t_{hyd} (Lamers and Cassinelli, 1999). In other words, the gas cools faster by radiative processes than by adiabatic expansion. Because of this, radiative cooling is calculated in the code using the first-order, time-implicit numerical scheme of Townsend (2009) as follows:

The rate of change of gas temperature dT/dt by radiative cooling is calculated as

$$\frac{dT}{dt} = -\frac{(\gamma-1) n_e \Lambda_H(T)}{k_B} - \frac{(\gamma-1) n_{CO} \Lambda_{CO}(T, T_{eq})}{k_B} \qquad [\mathrm{K/s}] \quad (2.4)$$

or after discretization

$$\frac{T^{n+1}(i,j,k) - T^n(i,j,k)}{\Delta t} = -\frac{(\gamma-1) n_e(i,j,k) \Lambda_H(T^{n+1}(i,j,k))}{k_B} - \frac{(\gamma-1) n_{CO}(i,j,k) \Lambda_{CO}(T^{n+1}(i,j,k), T_{eq}^{n+1}(i,j,k))}{k_B} \quad (2.5)$$

The indexes *i, j and k* indicate the numerical coordinates of the nested-mesh cells and the superscripts *n* and *n + 1* indicate values at times $t^n = n \cdot \Delta t$ and $t^{n+1} = (n+1) \cdot \Delta t$. The atomic mass unit is m_H and k_B is the Boltzmann constant. It is assumed that the electron number density n_e is 10^{-4} times the gas number density n_g if the temperature T is less than 8000 Kelvins and n_e is 10^{-3} times n_g if the temperature lies between 8000 and 12000 Kelvins (Bowen, 1988). It is also assumed that the number density of CO molecules n_{CO} is 10^{-4} times n_g. Radiative cooling $\Lambda_H(T)$ by collisional excitation or ionization of hydrogen by free electrons is taken into account using the following formulae (Black, 1981):

$$\Lambda_H(T) = \begin{cases} 7.5 \times 10^{-19} \exp(-118348/T), & \text{if } 4000 \text{ K} < T \leq 12000 \text{ K}. \\ 1.27 \times 10^{-21} T^{1/2} \exp(-157809.1/T), & \text{if } T > 12000K. \end{cases} \tag{2.6}$$

The function $\Lambda_H(T)$ has the physical units $[\text{erg} \cdot \text{cm}^3 \cdot \text{s}^{-1}]$. The function $\Lambda_{CO}(T, T_{eq})$, which has the same physical units as $\Lambda_H(T)$, is the radiative cooling by vibrational excitation of the CO molecule and is included as follows (Gail and Sedlmayr, 2013):

$$\Lambda_{CO}(T) = C_{10} \left[\exp(-3084/T) - \exp(-3084/T_{eq})\right] 3084 \, k_B \tag{2.7}$$

$$C_{10} = 10^{-6} \, k_B \, T \, exp(-3T^{-1/3} + 18.1) \qquad [\text{cm}^3 \cdot \text{s}^{-1}] \tag{2.8}$$

A formula describing the radiative equilibrium temperature T_{eq} is given in section 2.3. Given that vibrational excitation of CO is the most efficient cooling process (Woitke, Krueger, and Sedlmayr, 1996) in the range of temperatures (1500 K $\lesssim T \lesssim$ 3000 K) and number densities (10^7 cm^{-3} $\lesssim n_g \lesssim$ 10^{14} cm^{-3}) typical in the circumbinary envelopes of AGB stars (see chapter three), radiative cooling by other molecules is neglected.

Finally, it is considered an ideal gas composed of neutral atoms with a hydrogen to helium number ratio of 10 to 1. Therefore the gas has a ratio of specific heats $\gamma = 5/3$ and a constant mean molecular weight per particle $\mu = 1.27$. If ionization is taken into account, the total number density of free particles such as neutral hydrogen/helium, ions and electrons would change (along with γ and μ). In contrast, ignoring the effects of ionization will overestimate the temperature of the post-shocked regions since part of the energy input is used to ionise the gas rather than increasing its temperature (Vaidya et al., 2015). Nevertheless, the high density of the outflow makes the radiative cooling very efficient, reducing the effects of the shocks in the gas dynamics (see section 3.1).

2.2 The binary system

The binary system consists of an AGB star with a mass of $M_1 = 2.2$ M$_\odot$ and a secondary star on the main sequence with a mass of $M_2 = 0.8$ M$_\odot$. These values are taken from García-Segura, Villaver, Manchado, et al. (2016). We assume a fundamental-mode pulsation period of $P = 300$ d (days) for our AGB star. This period is within the range of values derived from infrared observations (Whitelock,

Feast, and Van Leeuwen, 2008; Chibueze et al., 2016). With the above values of mass and pulsation period, our AGB star has a radius of $R_1 = 316$ $R_\odot$ (Ostlie and Cox, 1986), which is approximately nine times the maximum mesh resolution. We adopt an orbital separation of $a = 674.3$ $R_\odot$ (3.13 au). This choice for the orbital separation ensures that the secondary star lies in a region where dust is not fully formed in the outflow, otherwise the gravitational effect of the secondary star in the outflow will be overshadowed by the radiation pressure on dust grains. Observations show that dust is formed at about two stellar radii (Norris et al., 2012) from the centre of the AGB star.

According to the Eggleton formula (Eggleton, 1983),

$$\frac{R_{RL}}{a} = \frac{0.49\, q_E^{2/3}}{0.6\, q_E^{2/3} + ln(1 + q_E^{1/3})}, \tag{2.9}$$

with a stellar mass ratio $q_E = M_1/M_2 = 2.75$, the radius of the Roche lobe R_{RL} for the primary star is 0.468 times the orbital separation a. Given that $a = 674.3$ $R_\odot$, $R_{RL} = 315.6$ $R_\odot$, the primary fills its Roche lobe (Paczyński, 1971).

The choice of the stellar mass for the primary in García-Segura, Villaver, Manchado, et al. (2016) was based on the fact that progenitor stars of bipolar PNe seems to be more massive than 2 $M_\odot$. This conclusion is supported by the distribution of bipolar PNe towards lower latitudes above the Galactic plane (Corradi and Schwarz, 1995) and their nitrogen enrichment compared to round or elliptical PNe (Stanghellini et al., 2006). The choice of the stellar mass for the secondary was based on observational studies which show that the mass ratio distribution $q = M_2/M_1$ for close binary stars (≤ 100 au $\sim 21,500$ $R_\odot$) has a maximum close to ~ 0.3 (Gullikson, Kraus, and Dodson-Robinson, 2016).

We also increase the mass of the companion to $M_2 = 1.6$ $M_\odot$, $M_2 = 2$ $M_\odot$ and $M_2 = 2.2$ $M_\odot$. These values are chosen to test whether systems with larger mass ratios $q = M_2/M_1$ form gravitationally-bound circumbinary rings (Shu, Lubow, and Anderson, 1979; Pejcha, Metzger, and Tomida, 2016) when radiation pressure on dust is taken into account.

The binary system is assumed to follow circular orbits, have synchronous rotation and their spin axes are perpendicular to the orbital plane. In other words, the Roche model is employed to study the dynamical interaction of the stellar wind with the binary star. The above assumptions are justified given that the timescales of tidal circularization and tidal synchronization in binary systems where the evolved stellar component has a deep convective envelope is much less than the timescale of the

AGB phase for an intermediate-mass star (Zahn, 1977).

2.3 Numerical approach for the primary star

For simplifying the hydrodynamic models, we assume that the AGB star is spherical (i.e. the surface of the primary star is not an equipotential surface). As an initial condition, the slow wind is setup spherically symmetric with respect to the centre of the AGB star. Although this condition may seems contradictory to what would be expected for the geometry of winds from binary stars, it is nevertheless a better approximation to real binaries than an initial, isotropic background gas with low density and in pressure equilibrium with the AGB star (Ricker and Taam, 2012; Staff et al., 2016). Given the above, the initial slow wind follows a velocity law of the form (Lamers and Cassinelli, 1999, chap. 2)

$$v(r_1) = v_0 + (v_\infty - v_0)(1 - R_1/r_1)^\beta, \qquad [\mathrm{km/s}] \quad (2.10)$$

where $v(r_1)$ is the wind velocity at a distance r_1 from the centre of the AGB star, whose radius is R_1. The parameter β describes the acceleration in the inner regions of the wind. In cool giant stars the wind accelerates more slowly, corresponding to values of $\beta \geq 1$. We take $\beta = 2.0$ but larger values have been used in literature (Khouri et al., 2014; Danilovich et al., 2015), see also e.g. Rau, Nielsen, et al. (2018) for warmer giant stars. The outflow velocity in AGB stars is typically 5 to 25 $\mathrm{km\,s^{-1}}$ (Ramstedt, Schöier, and Olofsson, 2009), for this reason we assign a terminal velocity of $v_\infty = 10\ \mathrm{km\,s^{-1}}$ and assume that the gas escapes from the stellar surface with a velocity $v_0 = 0.1\ \mathrm{km\,s^{-1}}$. Higher values of the surface velocity are computed in section 3.2. The initial density of the background gas is obtained using both the velocity field described in equation (2.10) and the initial mass-loss rate $\dot{M}$ of the AGB star in the continuity equation. For this purpose, the parametrization of Vassiliadis and Wood (1993)

$$\log \dot{M}(\mathrm{M_\odot\,yr^{-1}}) = -11.4 + 0.0123\ \mathrm{P\ (days)} \quad (2.11)$$

gives $\dot{M} \sim 2 \times 10^{-8}\ \mathrm{M_\odot\,yr^{-1}}$, for the adopted period of pulsation $P = 300$ d.

It is assumed as an initial condition that the background gas (whose density is $\sim 2.1 \times 10^{-14}\ \mathrm{g/cm^3}$ at the giant star-wind interface and $\sim 1.1 \times 10^{-18}\ \mathrm{g/cm^3}$ at the outer boundaries of the numerical domain) is in radiative equilibrium, thus its temperature T_{eq} at distances r_1 and r_2 from the centre of the

primary and secondary star, respectively, is (Djurasevic, 1986)

$$T_{\rm eq} = \left(\frac{1}{2}\right)^{\frac{1}{4}} \left(\left[1 - \sqrt{1 - \left(\frac{R_1}{r_1}\right)^2} \right] T_1^4 + \left[1 - \sqrt{1 - \left(\frac{r_s}{r_2}\right)^2} \right] T_s^4 \right)^{\frac{1}{4}}, \quad \text{[K]} \quad (2.12)$$

We assume an effective temperature of $T_1 = 3000$ K for the AGB star. This is a common temperature for Mira variable stars pulsating in their fundamental mode (van Belle, Thompson, and Creech-Eakman, 2002). We adopt an effective temperature $T_s = 5000$ K and a stellar radius $r_s = 1\ R_\odot$ for our secondary star of mass $M_2 = 0.8\ \mathrm{M}_\odot$, following the temperature-mass and mass-radius diagrams from Torres, Andersen, and Giménez (2010).

The wind from the AGB is driven by stellar pulsations coupled with radiation pressure on dust grains. Simple harmonic variations of the gas velocity $V(t)$ at the position $R(t)$ are employed to model the pulsations as follows

$$V(t) = \Delta u\ cos(2\pi t/P), \quad \text{[km/s]} \quad (2.13)$$

$$R(t) = R_0 + \frac{\Delta u}{2\pi/P}\ sin(2\pi t/P), \quad \text{[au]} \quad (2.14)$$

We assume an initial position of pulsation of $R_0 = 0.9\ R_1$. This value is chosen because pulsations in AGB stars are believed to be driven in the hydrogen-ionization zone, located approximately at $0.1 - 0.2\ R_1$ below the photosphere (Berlioz-Arthaud, 2003; Fadeyev, 2016). $\Delta u = 5\ \mathrm{km\,s^{-1}}$ and $P = 300$ d are the constant velocity amplitude and period of the pulsations, respectively. The former value is chosen from the range of radial velocities in AGB stars derived from observed Doppler-shifts of spectral lines (Lebzelter and Hinkle, 2002; Nowotny, Höfner, and Aringer, 2010).

From the equations of equilibrium (Applegate, 1988; Chandrasekhar, 1967, chap. 9), the temperature and density structure of the AGB surface layers are given by

$$T(r_1) = T_1 + \frac{1.79}{2.18} \frac{G M_1\, \mu\, m_{\rm H}}{k_{\rm B}} \left(\frac{1}{r_1} - \frac{1}{R_1} \right), \quad \text{[K]} \quad (2.15)$$

$$\rho(r) = \left[\left(\frac{1.79}{2.18} \right) \left(\frac{16\,\pi\, G M_1\, a\, c\, \mu\, m_{\rm H}}{3\, k_{\rm B}\, L_1\, \kappa} \right) \right] T^3(r_1), \quad \text{[g/cm}^3\text{]} \quad (2.16)$$

where G, a, c and L_1 are the gravitational constant, the radiation constant, the speed of light and the AGB star luminosity, respectively. Note that the law of opacity κ is given by the negative hydrogen ion H^- (Iben, 2013, chap. 7). Although we have the AGB stellar structure from García-Segura,

Villaver, Manchado, et al. (2016), it is preferable in our case to use the analytical expressions as in equations 2.15 and 2.16, since the grid resolution is limited, and the interpolation produces more numerical errors than the analytical formulae. The remaining AGB interior is assumed to be homogeneous and isothermal.

An essential process of the wind-driving mechanism in AGB stars is radiation pressure on dust grains. However the original code WALICXE3D does not include radiation forces in the gas-dynamic equations. Because of that, as another modification to the hydrodynamic code, we have considered the AGB star as a point source of radiation, thus the radiative acceleration takes the form:

$$a_{\rm rad} = \frac{k_{\rm D} L_1}{4\pi r_1^2 c} e_r, \qquad [{\rm m/s^2}] \quad (2.17)$$

where e_r is the unit radial vector and $k_{\rm D}$ is the dust opacity, which is approximated as (Bowen, 1988)

$$k_{\rm D} = \frac{k_{\rm max}}{1 + {\rm e}^{(T_{\rm eq} - T_{\rm cond})/\xi}}, \qquad [{\rm cm^2 \cdot g^{-1}}] \quad (2.18)$$

$T_{\rm cond} = 1500\ K$ is the condensation temperature and its range spreads over $\xi = 200\ K$. These values are selected because the most abundant dust species in carbon-rich stars, namely amorphous carbon and silicon carbide (Rau, Paladini, et al., 2015), have condensation temperatures between 1300 and 1700 K, approximately (Lodders and Fegley, 1995; Leisenring, Kemper, and Sloan, 2008). Carbon-rich AGB stars are observed to have winds with expansion velocities ranging from 5 to 30 $\rm km\,s^{-1}$, with a peak distribution between 10 to 15 $\rm km\,s^{-1}$ (Loup et al., 1993). Based on this, the maximum value of dust opacity $k_{\rm max}$ is a constant adjusted to give expansion velocities of the slow wind of $\sim 10-20$ $\rm km\,s^{-1}$ towards the pole, where the hydrodynamical interaction of the wind with the secondary star is minimum. The AGB luminosity L_1 is calculated from the stellar effective temperature, radius and pulsation properties

$$L_1 = \pi a c T_1^4 \left(R_1 + \frac{\Delta u}{2\pi/P} sin(2\pi t/P) \right)^2, \qquad [{\rm erg \cdot s^{-1}}] \quad (2.19)$$

2.3.1 Numerical approach for the secondary star

In our simulations the secondary star is not resolved; it is a point source, since its radius (equal to one solar radius) is smaller than a grid cell of our computational mesh. Therefore, its gravitational potential would induce extremely large accelerations to the nearby gas and, consequently, infinitesimal

time-steps. For avoiding this, we smoothed the potential following Ruffert (1993)

$$\phi(r_2) = \frac{-GM_2}{\sqrt{r_2^2 + \varepsilon^2\delta^2 \mathrm{e}^{-(r_2/\varepsilon\delta)^2}}}, \qquad [\mathrm{erg}\cdot\mathrm{g}^{-1}] \quad (2.20)$$

The smoothing length δ is equal to the size of one cell in the innermost mesh and r_2 is the distance to the secondary star of mass M_2. Following Staff et al. (2016) the parameter ε is equal to 3, which ensures a finite gravitational potential at the secondary star position. With this value for ε, the smoothed potential is identical to the true potential at ~ 7 cell widths from the secondary star (see discussion). Lower values for ε produce similar results at the cost of smaller time-steps, which increases the total computational time.

Chapter Three

Results

3.1 3-D numerical results

The simulations are first run during a couple of orbits until they reached a steady-state configuration. After that, we calculate 40 orbital cycles to make a time average of the density and outflow velocity of the stellar wind, in order to obtain an axisymmetric, 2-dimensional structure. The required number of cycles was empirically determined after comparing the averaged density and velocity distributions in the wind at different times. In other words, the averaged outflow do not change significantly between 40 and 100 orbital cycles, which is not the case when comparing the structure at 20 and 40 cycles.

Table 3.1 shows different input parameters such as orbital separation a, mass of the stellar components M_1 and M_2, mass ratio q, orbital period P_{orb} and maximum dust opacity k_{max} for each binary system. The Model 1 (our fiducial model) is shown in the first line.

Table 3.1 Input parameters for the binary models.

Models	a (au)	M_1 ($M_\odot$)	M_2 ($M_\odot$)	$q = M_2/M_1$	$P_{\rm orb}$ (yr)	$k_{\rm max}$	Remarks
1	3.1	2.2	0.8	0.36	3.2	5.6	Fiducial model in RLOF
2	3.8	2.2	0.8	0.36	4.2	5.6	
3	4.4	2.2	0.8	0.36	5.3	5.6	
4	4.4	2.2	1.6	0.73	4.7	6.6	
5	4.4	2.2	2.0	0.91	4.5	8.5	
6	4.4	2.2	2.2	1.0	4.4	8.8	
7	3.1	2.2	0.8	0.36	3.2	5.6	Adiabatic simulation. Otherwise, Model 1

Table 3.2 Mass-loss rates for the binary models resulting from our calculations.

Models	$\dot{M}$ $(M_\odot yr^{-1})$	Polar outflow velocity (km/s)
1	5.8e-5	12.5
2	1.6e-6	11.4
3	1.2e-7	11.7
4	4.4e-6	8.5
5	1.8e-5	16.0
6	3.2e-5	15.4
7	7.2e-4	20.8

The computed mass-loss rates of each model are shown in Table 3.2. The mass-loss rates are calculated through a spherical surface of radius 4300 $R_\odot$ (20.0 au), close to the outer boundaries of the simulation, where the out-flowing material is supersonic.

Figure 3.1 shows a density snapshot of Model 1 at the orbital plane (XY plane) and Figure 3.2 shows its time-averaged density (top panel) and outflow velocity (bottom panel) at the XZ plane. We find that mass loss in the binary star occurs mainly through the outer Lagrangian point L_2. The resultant outflow develops into a spiral plume at low distances from the binary, that is quickly smoothed out by shocks and becomes an excretion disk at larger distances from the stars. This leads to the formation of an outflow structure with an equatorial density enhancement, i.e., with a large pole-to-equator density ratio, as also shown in Chen et al. (2017).

Figure 3.3 shows the time-averaged density (top panel) and outflow velocity (bottom panel) profiles as functions of the coordinate X, which indicates the distance from the centre of mass. These profiles are calculated in the orbital plane to study mass-loss sensitivity to orbital separation. Far from the barycentre ($\gtrsim 6$ au), the gravitational potential of the binary system approximates that of a single star. Consequently, at distances larger than ~ 6 au the outflow in these models follows similar power-law distributions of density and an identical velocity law (see equations 3.3 and 3.4 of subsection 3.2). Lastly, one can see in Figure 3.3 that the gas has a higher increase of velocity (and by conservation of mass, a higher decrease in density) between ~ 3 and ~ 8 au, compared to more distant regions. This is the consequence of transfer of linear momentum, from the gas ejected through the equator to the already present spiral plume. In fact, the greater the distance to the barycentre, the less linear

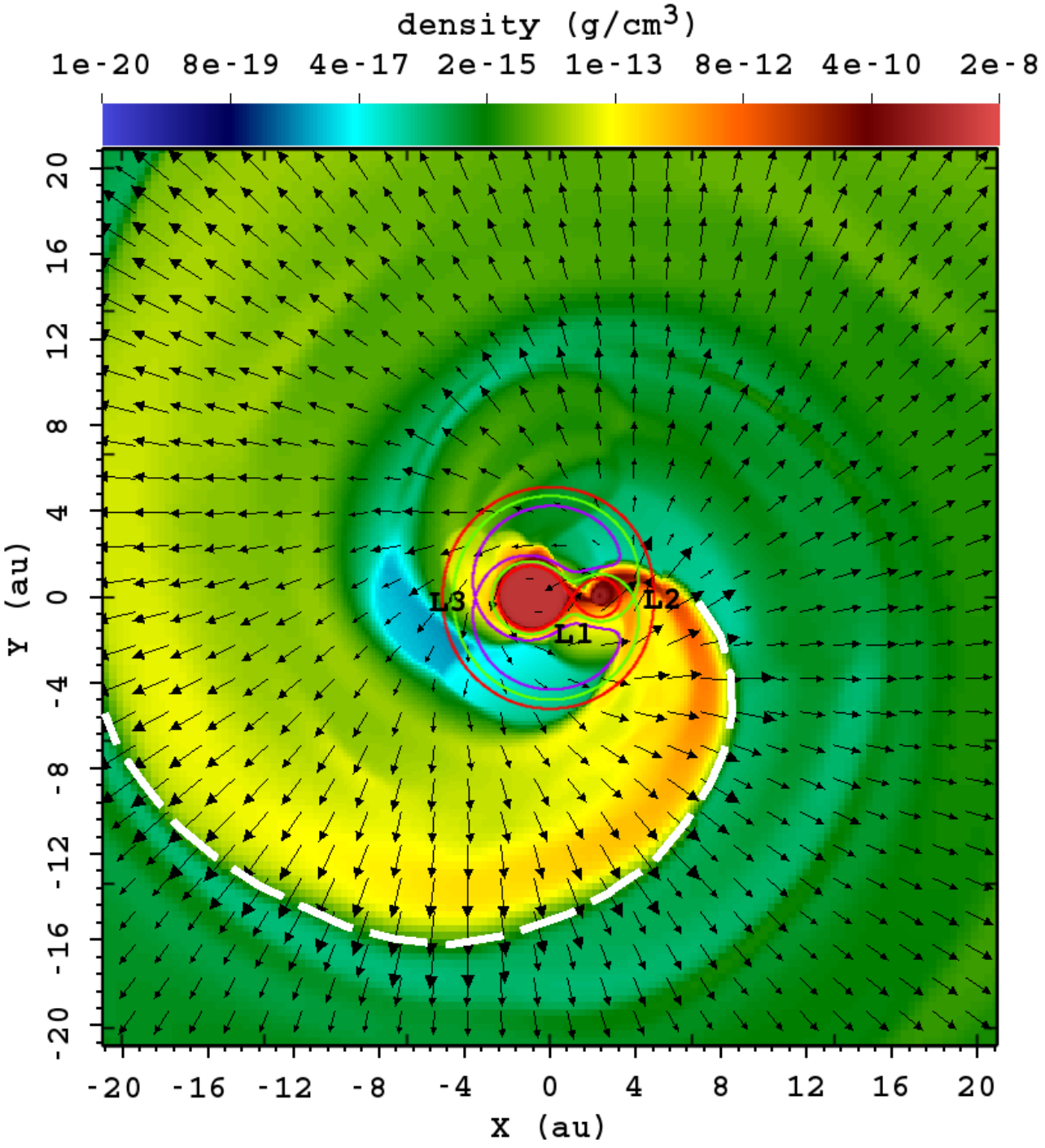

Figure 3.1 Density map in logarithmic scale at the XY plane for our fiducial model (Model 1). The white dashed line indicates the spiral plume. Black arrows represent the velocity field. The centre of mass (barycentre) is located at (0, 0). Also shown are the equipotential curves (Red, green, violet) and the Lagrangian points L_1, L_2 and L_3.

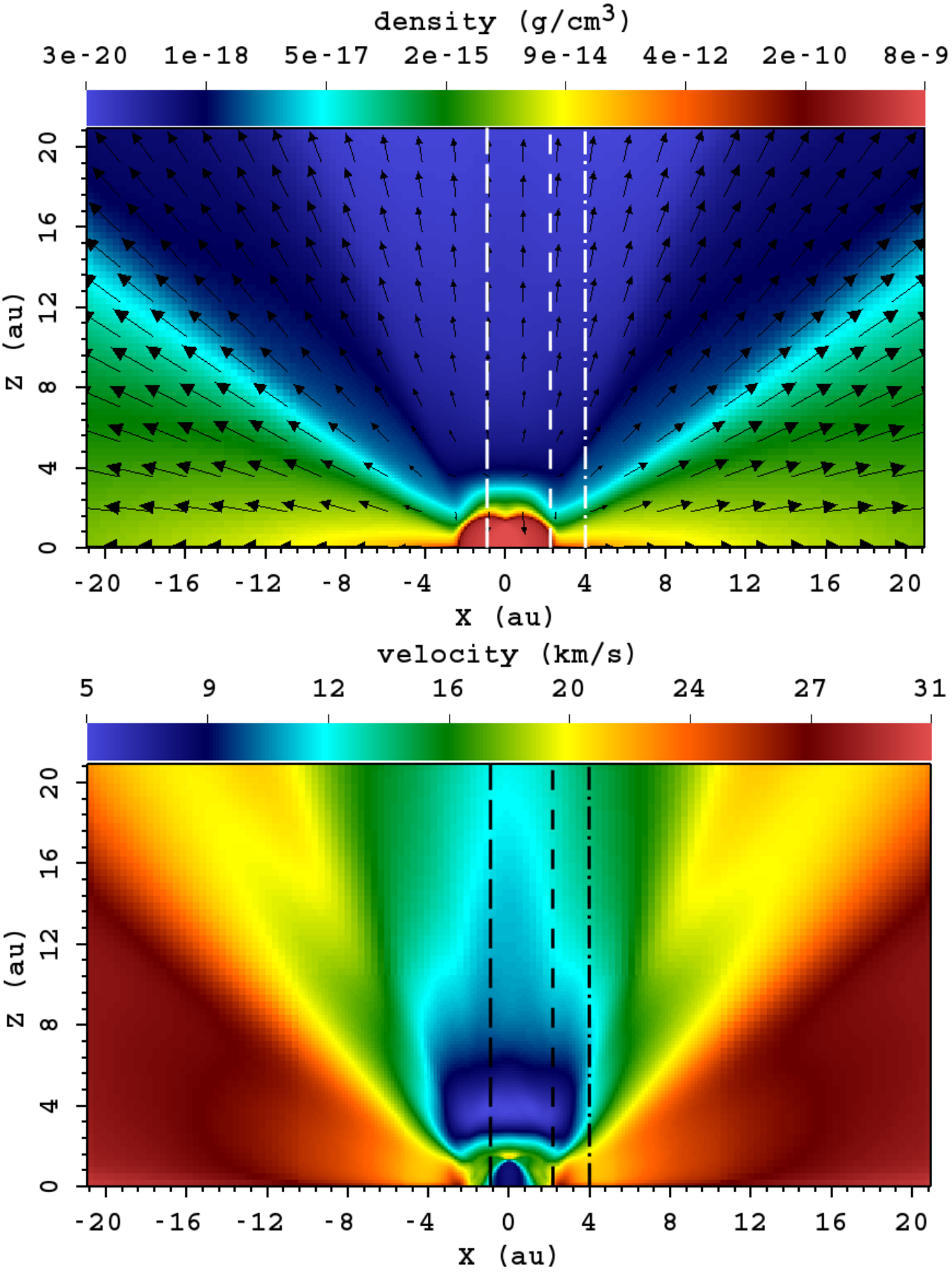

Figure 3.2 Time-averaged density (top) and outflow velocity (bottom) maps in logarithmic and linear scale, respectively, for our fiducial model at the XZ plane. Black arrows represent the velocity field. From left to right, the vertical lines indicate the position of the primary star (long dashed), the position of the secondary star (short dashed) and the position of the L_2 point (dot-dash).

momentum is transferred.

Figure 3.4 shows the time-averaged density (top panel) and outflow velocity (bottom panel) profiles as functions of the colatitude angle θ, which goes from 0° at the pole to 90° at the XY plane (Figure 3.5). These two profiles are calculated at 20 au from the barycentre of the system, in the outermost mesh. From Figure 3.4 one can recognized three distinct regions in the outflow of Model 1: the first of them comprises the polar region (colatitude θ between 0° and 30°), the second (which is called the transition region in this thesis) goes from 30° to 60° and the third is the equatorial region, which goes from 60° to 90°. The equatorial region is filled with gas ejected by the binary system through the Lagrangian points L_3 and L_2. Some of the ejected gas is deviated towards the transition region due to the collision with previously expelled material. While moving away from the orbital plane, the gas in the transition region makes work against the gravity of the binary stars. For that reason, the outflow velocity decreases when moving from $\sim 60°$ to $\sim 40°$ in colatitude. Finally, the gas which fills the polar region was ejected from the primary star by the combined action of stellar pulsations and radiation pressure on dust grains. In other words, the gas in the polar region does not come from the flux of material through the Lagrangian points, however this polar gas collides with the faster material in the transition region and is accelerated. Because of this, the outflow velocity increases at $\sim 30°$ of colatitude. The density of the three regions is markedly different as a consequence of material being ejected preferentially along the orbital plane. Indeed, the pole-to-equator density ratio reaches a maximum value of $\sim 10^5$ in Model 1, where Roche-Lobe Overflow (RLOF) occurs. On a final note, the three regions of the outflow are also visible, although not as evident, in the Models 2 and 3, where one can see that the equatorial region is thinner.

Models 1, 2 and 3 have equal stellar masses but different orbital separations. Contrary to Model 1, in which mass is lost through the Lagrangian point L_1 directly from the photosphere of the donor star, it is the AGB wind that flows through the point L_1 in Models 2 and 3. In consequence when the orbital separation is smaller, the outflow structure changes in the following ways. First, at distances from the centre of mass greater than ~ 4 au, the circumbinary gas is denser in Model 1 with respect to Models 2 and 3 at the orbital plane, as shown in the top panel of Figure 3.3. This is caused by a larger mass-loss rate from the binary system through the outer Lagrangian points. Second, a stronger deviation from spherical symmetry in the mass-loss geometry is produced, or in other words, the pole-to-equator density ratio increases up to $\sim 10^5$, as it is shown in the top panels of Figure 3.2 and 3.4.

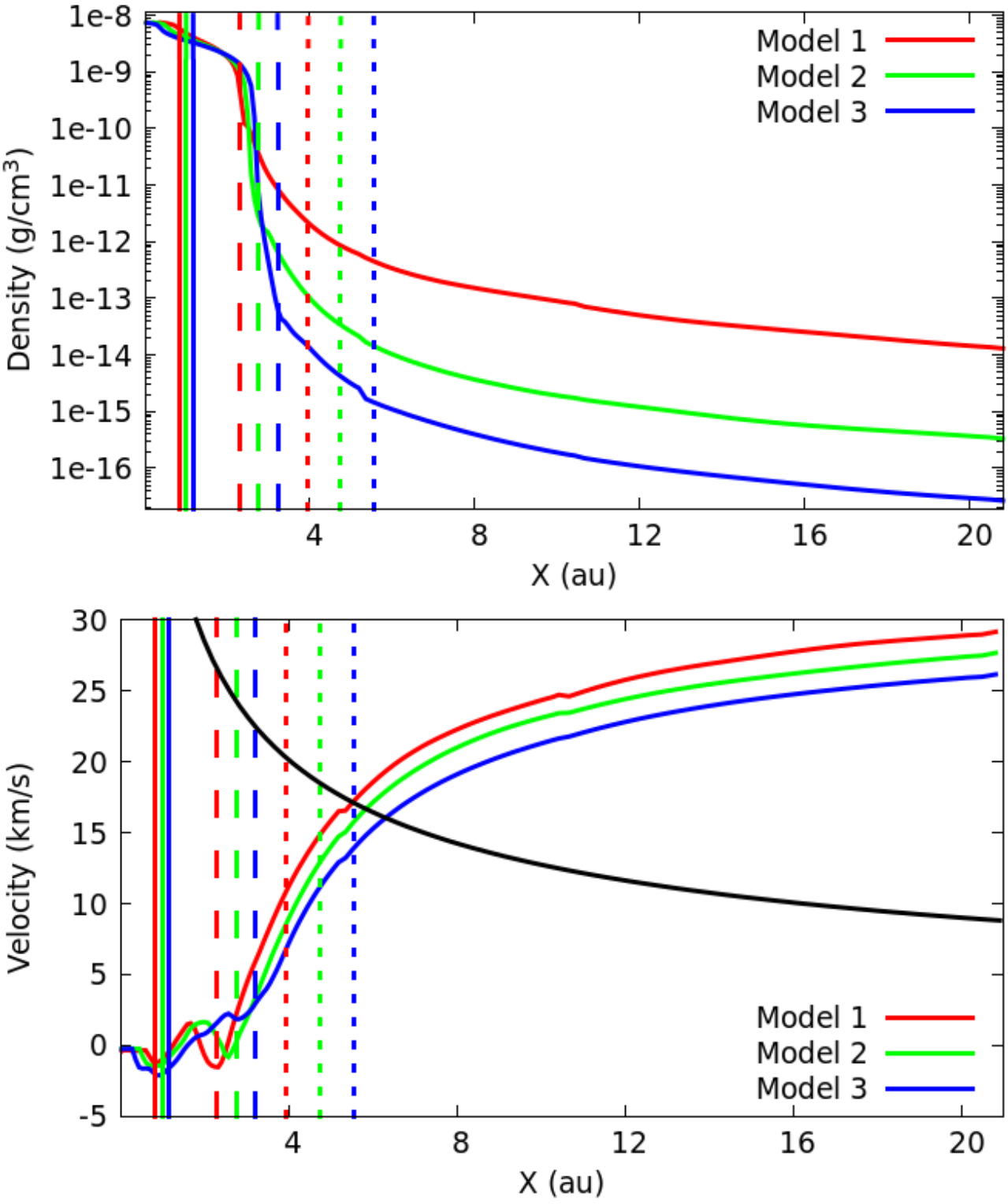

Figure 3.3 Time-averaged density (top) and outflow velocity (bottom). The horizontal axes indicate the distance from the centre of mass. The vertical lines, linked to their respective model by the colour, indicate the position of the secondary star (solid), the position of the primary star (long dashed) and the position of the L_2 point (short dashed). The black line shows the escape velocity of the binary systems.

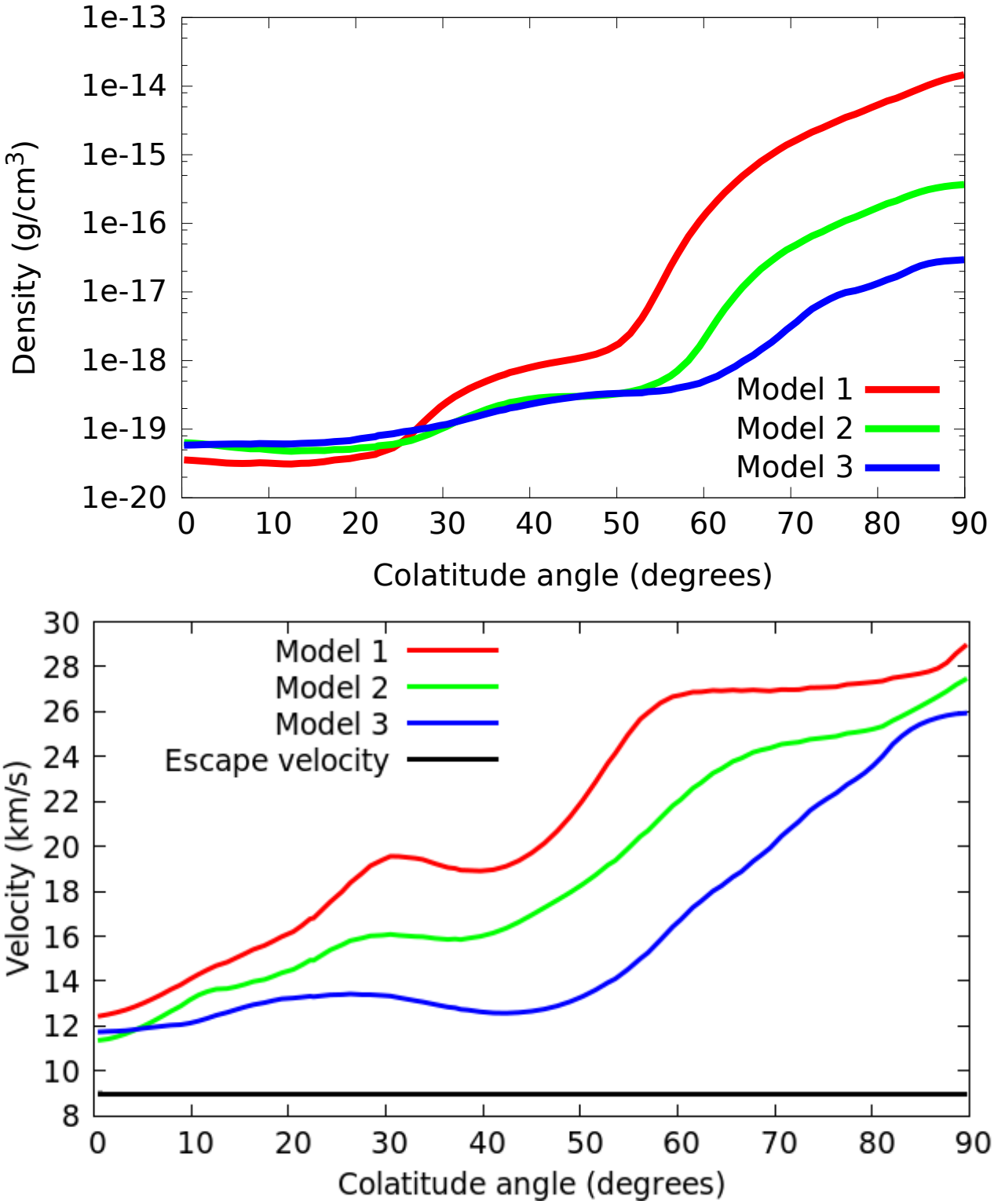

Figure 3.4 Time-averaged density (top) and outflow velocity (bottom) at 20.0 au from the barycentre of the system for Models 1, 2 and 3. The horizontal axes indicate the colatitude angle which goes from 0° at the pole to 90° at the XY plane. The escape velocity of the binary systems (black horizontal line) is ~ 9 km/s.

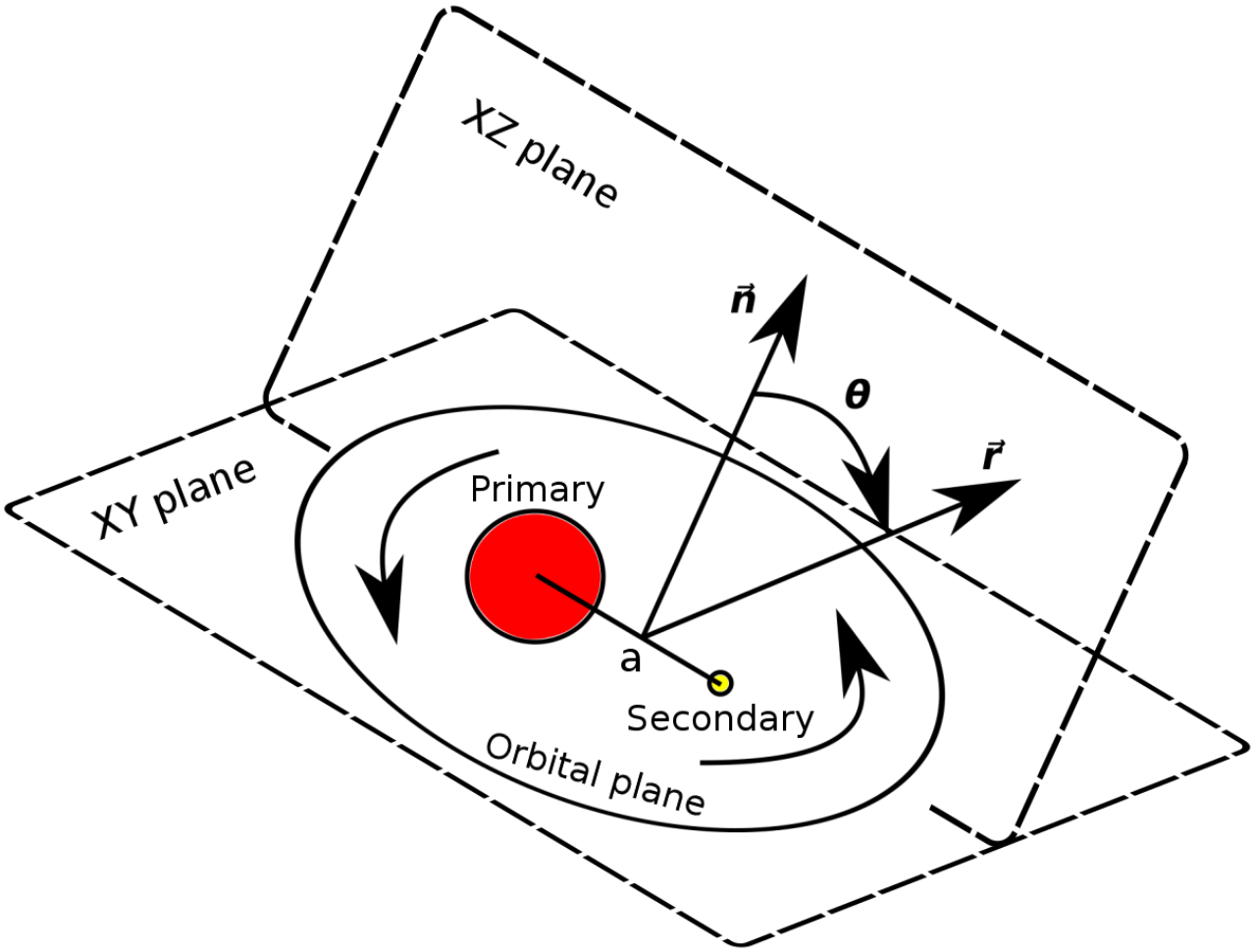

Figure 3.5 Colatitude angle θ between the position vector $\vec{r}$ of each mesh cell and the unit normal vector $\vec{n}$ to the orbital plane. The orbital separation a is indicated by the line segment joining the stars.

This is caused by a stronger gravitational focusing of the winds towards the companion star. Third, the outflow is faster (bottom panels of Figure 3.3 and 3.4). This is a consequence of the momentum imparted to the wind by the secondary star with a faster orbital motion. The above results give rise to an increase of the mass-loss rate (Table 3.2). The escape velocity of Models 1, 2 and 3 is also shown in the bottom panel of Figure 3.3, where one can see that at distances from the barycentre beyond ~ 7 au the gas ejected through the Lagrangian points L_2 and L_3 is not gravitationally bounded to the binary stars. This is not surprising given that even without the help of radiation pressure on dust grains, the spiral plume from a binary system with a stellar mass ratio $q = M_2/M_1 = 0.36$ (Table 3.1) becomes unbound (Shu, Lubow, and Anderson, 1979; Pejcha, Metzger, and Tomida, 2016).

Models 4, 5 and 6 have equal orbital separation but different companion stellar mass and maximum value of dust opacity k_{max}. This produces the following changes in the outflow structure when the mass ratio $q = M_2/M_1$ increases towards unity. First, more material is lost through the outer Lagrangian points (L_3 and L_2) and less gas reaches the distant polar regions, as a consequence the pole-to-equator density ratio also increases (top panel of Figure 3.6). Second, the mass-loss rate is enhanced, as can be seen in Table 3.2. If both the companion stellar mass and the maximum dust opacity $k_{\max}$ increase, then the outflow velocity also increases as shown in the bottom panel of Figure 3.6.

At distances beyond ~ 5 au from the barycentre in Model 4 and beyond ~ 8 au in Models 5 and 6, the time-averaged outflow velocity at the orbital plane becomes larger than the escape velocity relative to the barycentre, as shown in Figure 3.7. In Models 4, 5 and 6 the stellar mass ratios are equal to 0.73, 0.91 and 1, respectively. Therefore if radiation pressure on dust is included, the gas ejected through the Lagrangian L_2 point does not form an outer ring of gravitationally bound material when $q = M_2/M_1 = 0.73$ (Figure 3.8) or when $q = M_2/M_1 > 0.78$, as seen in Figures 3.9 and 3.10.

For comparison, Model 7 (Table 3.1) is computed without radiative cooling. On the one hand, due to a larger gas thermal pressure, less material falls inward in the accretion disc surrounding the secondary star. As a result, the flux of matter through the Lagrangian point L_2 increases, as can be seen in the top panel of Figure 3.11. On the other hand, the outflow velocity at the orbital plane (bottom panel of Figure 3.11) is not affected significantly, given that the gas dynamics is dominated by the linear momentum transferred to the spiral plume, and the radiative pressure on dust grains (note that in Equations 2.12, 2.17 and 2.18 of section 2.3, the gas temperature is absent, therefore the radiative

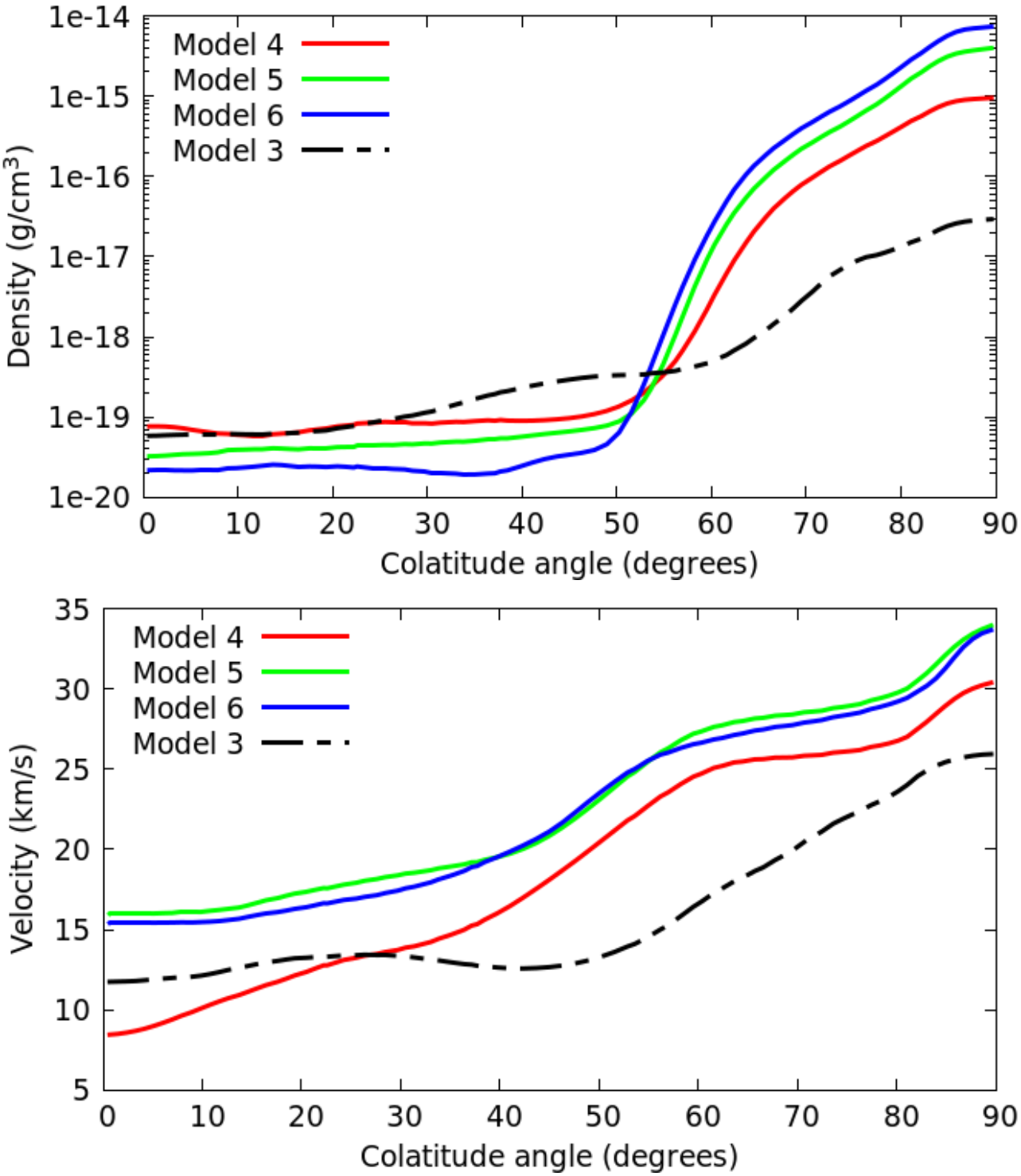

Figure 3.6 Time-averaged density (top) and outflow velocity (bottom) at 20.0 au from the barycentre of the system for Models 3, 4, 5 and 6.

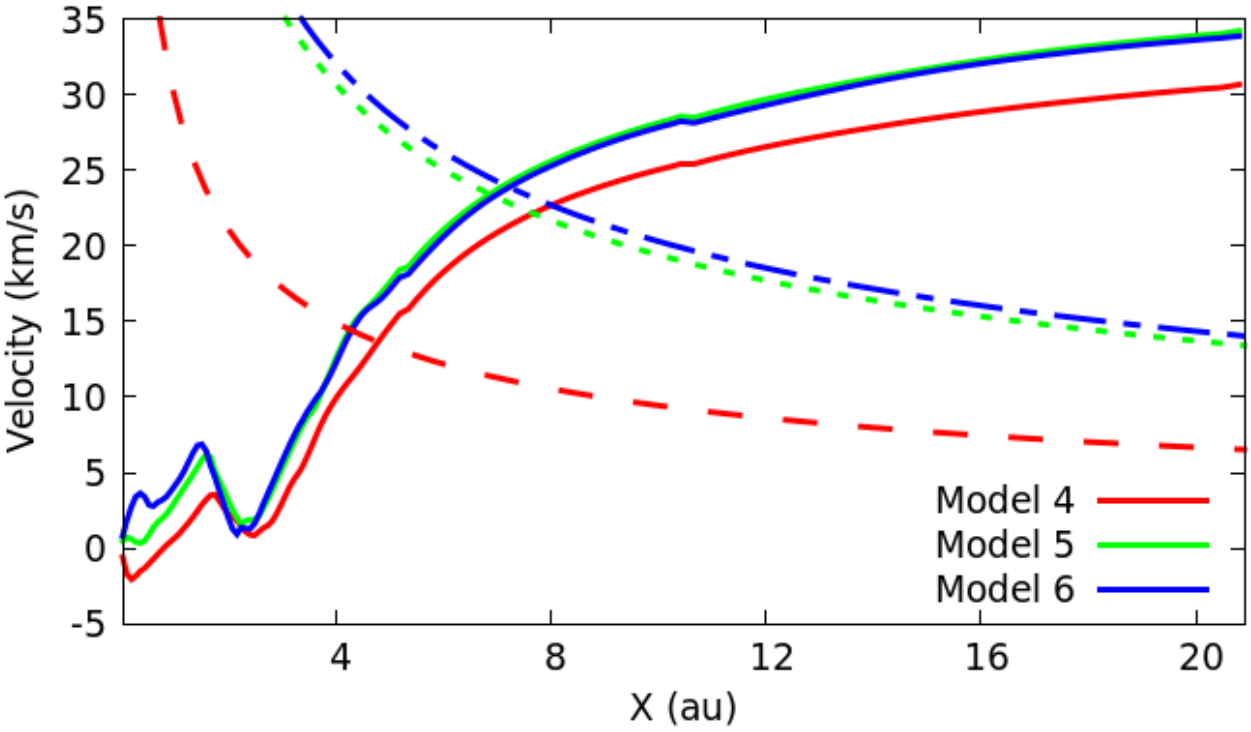

Figure 3.7 Time-averaged outflow velocity, as function of the X coordinate, for Models 4, 5 and 6. The escape velocity, linked to its respective model by colour, is also shown.

acceleration is the same for Models 1 and 7). In addition, the gas behind the pulsation-induced shock can no longer radiate its internal energy and expands adiabatically before the next shock appears. As a consequence, the gas velocity increases in the low-colatitude (polar) regions (bottom panel of Figure 3.12). Because of that, the gravitational focusing of the AGB wind towards the orbital plane is underestimated (Gawryszczak, Mikołajewska, and Różyczka, 2002) since there is a larger thermal pressure that works against gas compression (top panel of Figure 3.12).

3.2 Analytical fits

Finally, we make a curve fitting to the profiles to find analytical expressions of the outflow structure. The variation of density and outflow velocity with the colatitude angle θ (Figure 3.5) in the stellar wind is described using several Gaussian functions in equations 3.1 and 3.2, respectively. In these equations, density and outflow velocity are given by the coefficient s near the symmetry axis and by b_i at colatitude angle c_i. The coefficient d_i represents the width of the Gaussian functions. Table 3.3 shows numerical values of the coefficients for the Models. Density ($\mathrm{g\,cm^{-3}}$) and outflow velocity ($\mathrm{km\,s^{-1}}$) as functions of both distance r (in au) from the barycentre and colatitude angle θ (in degrees) are given in equations 3.3 and 3.4, respectively. In the former equation the dependence on distance is

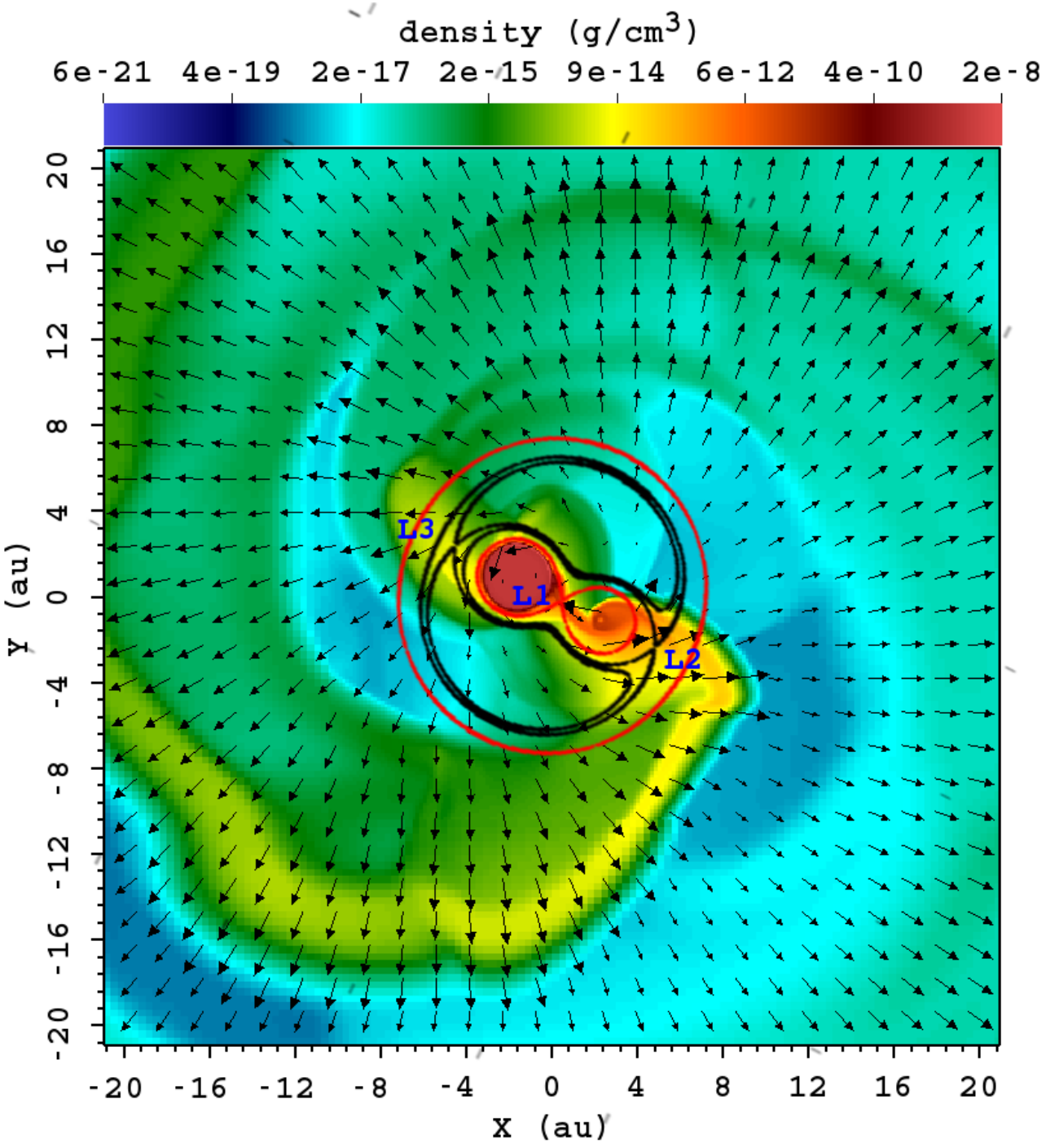

Figure 3.8 Density map in logarithmic scale at the XY plane for Model 4. Black arrows represent the velocity field. The barycentre is located at (0, 0). Also shown are the equipotential curves (Red and Black) and the Lagrangian points L_1, L_2 and L_3.

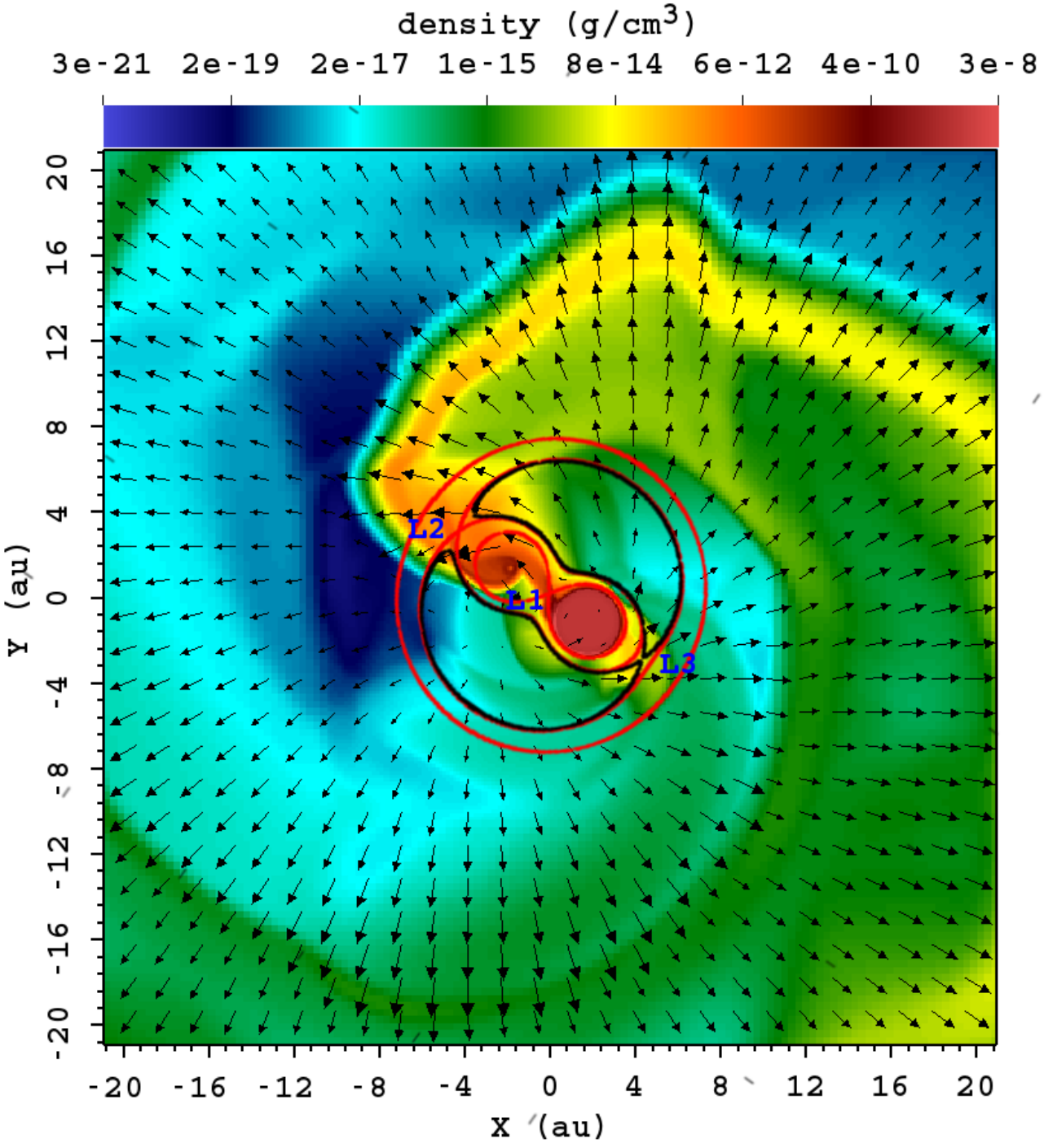

Figure 3.9 Same as Fig. 3.8 for Model 5.

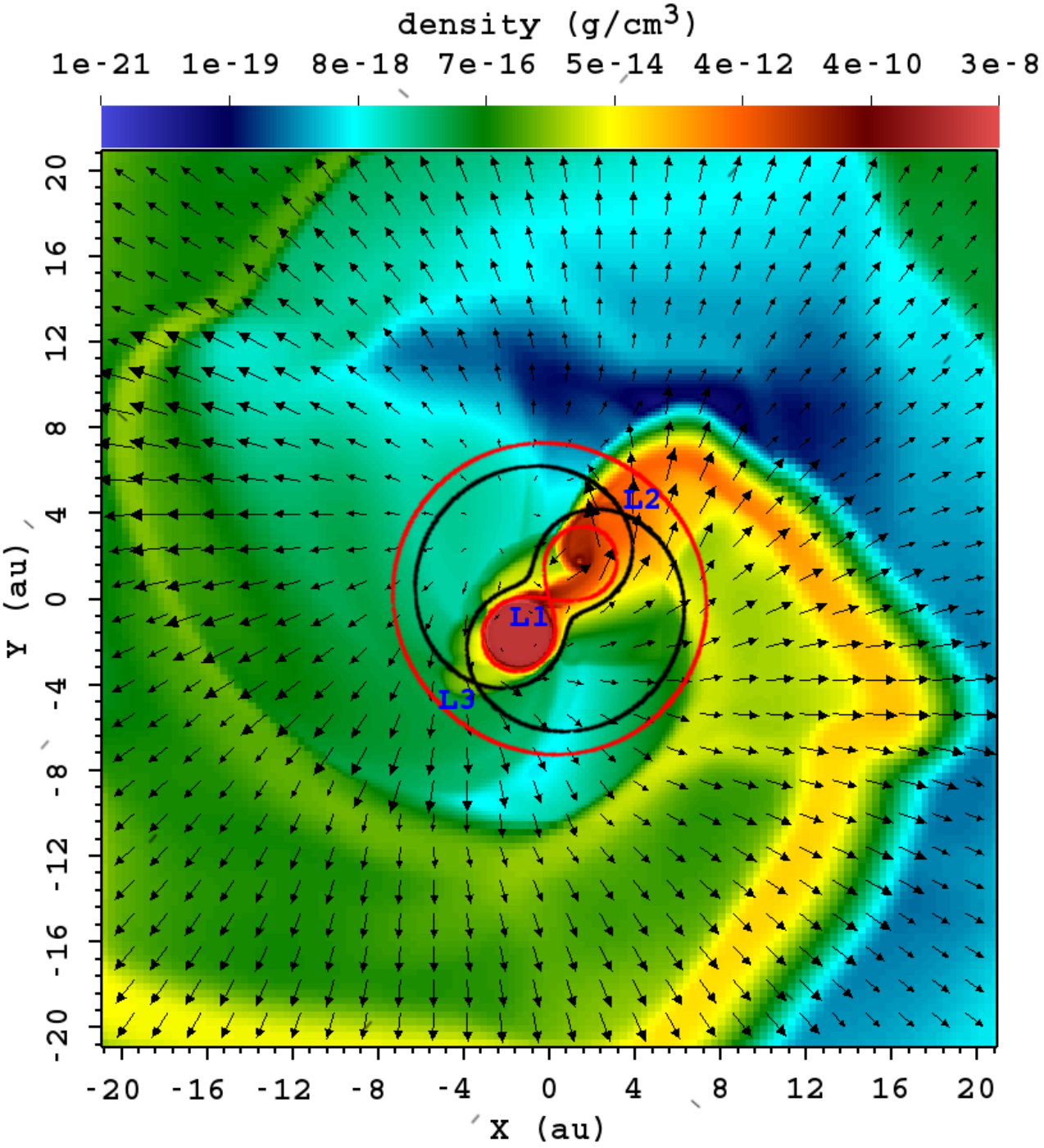

Figure 3.10 Same as Fig. 3.8 for Model 6.

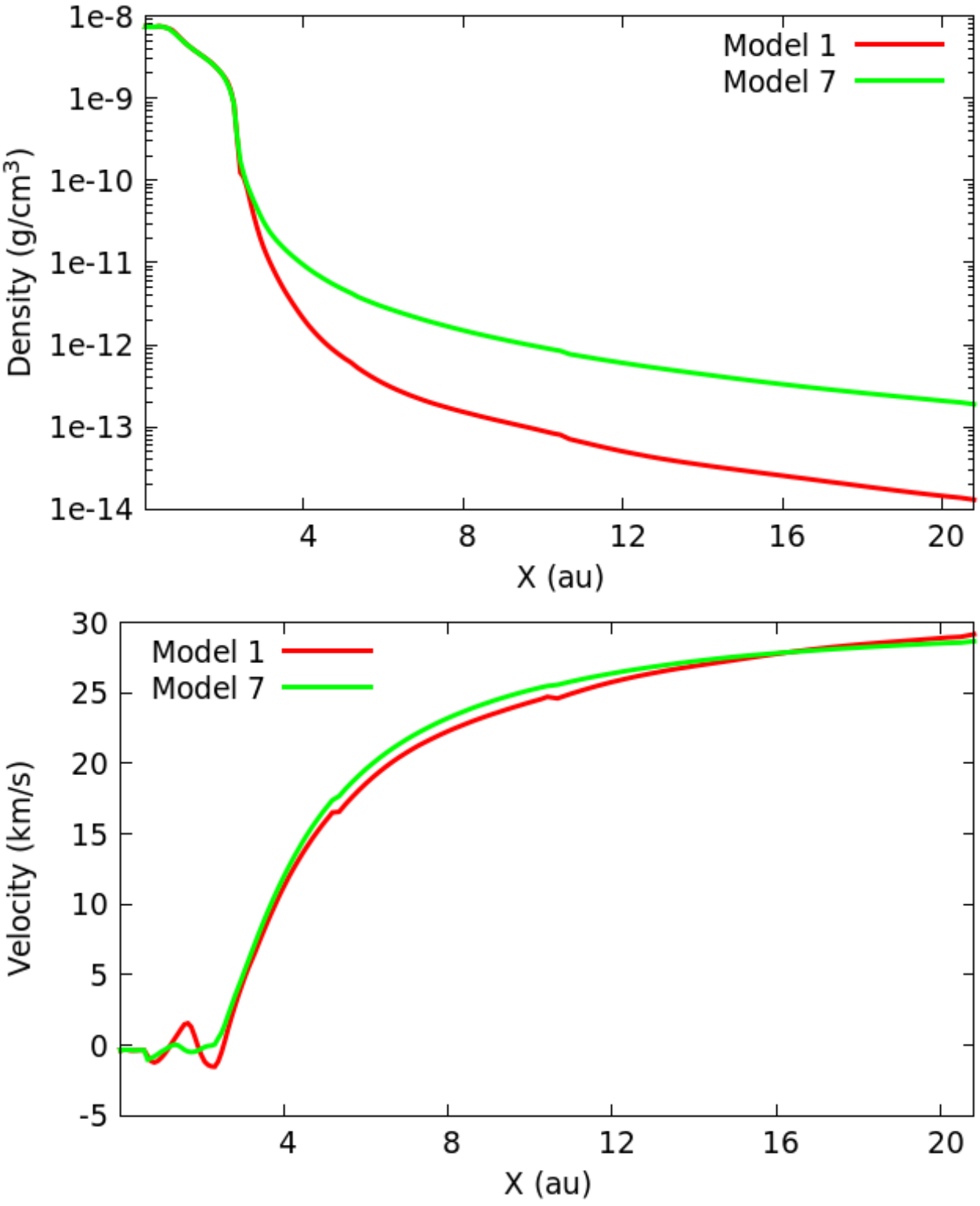

Figure 3.11 Time-averaged density (top) and outflow velocity (bottom) for Models 1 and 7.

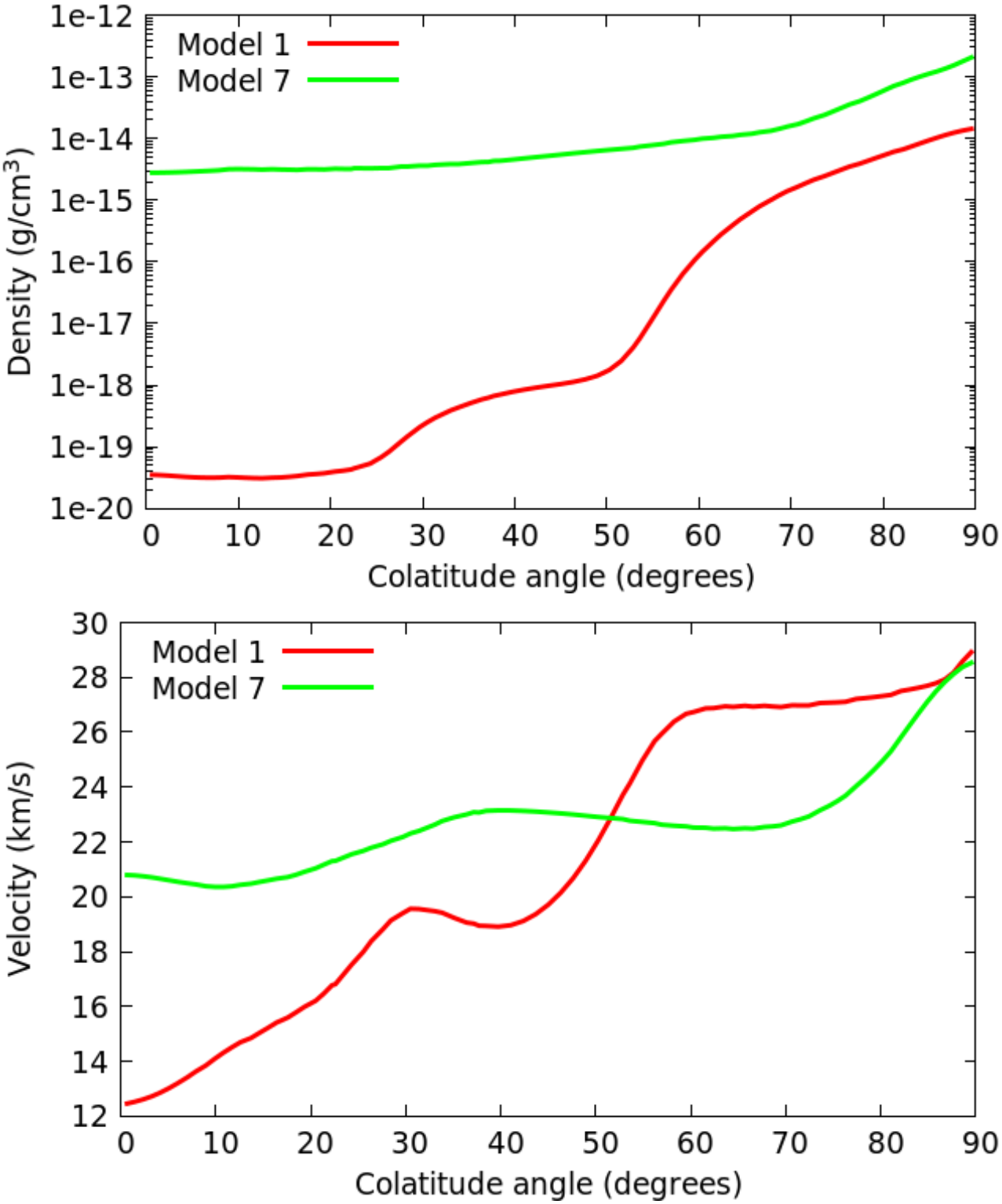

Figure 3.12 Time-averaged density (top) and outflow velocity (bottom) at 20.0 au from the barycentre for Models 1 and 7.

fitted to a power-law function $\rho \propto r^{-f}$. While in the latter equation, we use a velocity field similar to that described in equation 2.10; however we replace the constant surface velocity v_0 by equation 3.2.

$$\Psi(\theta) = s + \sum_{i=1}^{5} b_i \mathrm{e}^{-(\theta - c_i)^2/d_i^2}, \tag{3.1}$$

$$\vartheta(\theta) = s + \sum_{i=1}^{5} b_i \mathrm{e}^{-(\theta - c_i)^2/d_i^2}, \tag{3.2}$$

$$\frac{\rho(r,\theta)}{\rho_{\mathrm{ref}}} = \Psi(\theta)\left(\frac{r_c}{r}\right)^f, \tag{3.3}$$

$$\frac{v(r,\theta)}{V_{\mathrm{orb}}} = \vartheta(\theta) + (\vartheta(\theta) - v_\infty) * \left(\frac{r_c}{r} - 1\right)^f, \tag{3.4}$$

Given that these expressions could be used as initial conditions characterizing the circumbinary medium in simulations of aspherical PNe at larger spatial dimensions, we choose the length scale parameter r_c as far from the binary star as possible, in a region where the outflow is unbound and its morphology has not changed considerably as compared to inner regions. Taking the above into account, $r_c = 20.0$ au. The parameter v_∞ is the wind terminal velocity (not to be confused with v_∞ defined in section 2.3), which is determined from the outflow at the outer boundaries of the numerical domain for each model. $V_{\mathrm{orb}} = (2\pi a)/P_{\mathrm{orb}}$ and $\rho_{\mathrm{ref}} = \dot{M}/(4\pi r_c^2 V_{\mathrm{orb}})$ are, respectively, velocity and density scale factors. The orbital separation a and the orbital period $\mathrm{P_{orb}}$ for each model are given in Table 3.1, while the total mass-loss rates $\dot{M}$ are shown in Table 3.2.

Table 3.3 Coefficients for the analytical fits of the outflow structure

Function	s	b_1	c_1	d_1	b_2	c_2	d_2	b_3	c_3	d_3	b_4	c_4	d_4	b_5	c_5	d_5	f
$\rho_1(r,\theta)$	$2.9e-5$	$5.4e-4$	39	8.2	$8e-4$	49	7	1.1	72	7.9	3.5	80.5	6.5	11.6	90	6.2	2.55
$v_1(r,\theta)$	0.42	$5.9e-2$	13.3	7.8	0.2	30.4	11.4	0.21	57.8	13.3	0	0	0	0.54	90	37.3	1
$\rho_2(r,\theta)$	$1.5e-3$	$4.1e-4$	0	6	$7.1e-3$	42.5	10.5	$8.8e-3$	58.5	9	1.48	74.5	7.9	10.7	90	10.2	2.55
$v_2(r,\theta)$	0.42	$5.2e-2$	11.4	6.5	0.16	28.1	13	0.25	54.3	15.5	0.23	68.2	11.1	0.58	90	18.6	1
$\rho_3(r,\theta)$	$2.2e-2$	$5.1e-3$	27	7	$9.2e-2$	49	14.5	0.15	67	10	3.7	79	8	10.1	90	7	2.5
$v_3(r,\theta)$	0.47	$7.7e-2$	26.1	16.1	0	0	0	0	0	0	0.2	66.2	14.4	0.57	90	17.9	1
$\rho_4(r,\theta)$	$5e-4$	$3.2e-4$	0	8	$5.1e-4$	35	22	$1.8e-3$	58	8.3	0.62	71.6	6.4	10.8	90	10.9	2.45
$v_4(r,\theta)$	0.24	0.16	22.4	19.9	0	0	0	0.67	66.5	27.2	$8.2e-2$	78.1	6.4	0.5	90	8.2	1
$\rho_5(r,\theta)$	$9.5e-5$	0	0	0	$4.3e-5$	30	15.9	$1.2e-4$	50	8.9	0.63	72.1	6.9	11.2	90	9.5	2.6
$v_5(r,\theta)$	0.54	0	0	0	$6.9e-2$	29	14.5	0.41	64.5	20	0.18	80	9.5	0.45	90	7.5	1
$\rho_6(r,\theta)$	$3.2e-5$	$9.9e-6$	17	10	0	0	0	$3.6e-5$	51	8	0.66	72	7	12.1	90	9.3	2.45
$v_6(r,\theta)$	0.52	0	0	0	$6.7e-2$	34	16.2	0.19	55.7	14	0.46	83.2	26.1	0.19	90	5.6	1
$\rho_7(r,\theta)$	0.2	$2.9e-2$	20	15	0	0	0	0.33	60	20	0.43	71	10	9.4	90	10.5	2.1
$v_7(r,\theta)$	0.7	$1.7e-2$	0	7	$9.2e-2$	39	16	0	0	0	$6.7e-2$	65	17	0.27	90	12	1

Figure 3.14 and Figures 1 to 6 in the appendix show the analytical fit to the time-averaged density and outflow velocity profiles, as functions of the colatitude angle, for our models using equations (3.1) and (3.2), respectively.

Finally, Table 3.4 shows the time-averaged density and outflow velocity of the stellar wind of additional models. For each of these models the initial wind velocity v_0 at the surface of the AGB star is different, while the input parameters such as orbital separation, stellar masses and maximum dust opacity are equal to those in our Model 1 (Table 1). Values for density and outflow velocity were taken at a fixed distance of 20.0 au from the barycentre and at different colatitude angles θ. As can be seen in Table 3.4 and in Figure 3.13, the outflow hydrodynamical structure is not modified considerably with different values for v_0.

Table 3.4 Density and outflow velocity of the stellar wind for models with different initial wind velocities at the surface of the AGB star.

	Model with $v_0 = 0.1$ km s^{-1}		Model with $v_0 = 1.0$ km s^{-1}		Model with $v_0 = 5.0$ km s^{-1}	
Colatitude angle θ	ρ (g cm^{-3})	v (km s^{-1})	ρ (g cm^{-3})	v (km s^{-1})	ρ (g cm^{-3})	v (km s^{-1})
5.2	4.5e-20	10.9	4.4e-20	10.9	4.2e-20	11.0
14.5	4.3e-20	15.3	4.2e-20	15.4	3.8e-20	15.5
24.5	6.1e-20	18.1	6.1e-20	18.1	5.7e-20	18.3
34.8	4.1e-19	19.0	4.1e-19	19.0	4.0e-19	19.2
45	2.0e-18	17.9	2.0e-18	17.9	1.9e-18	18.1
55.2	2.9e-17	23.8	2.9e-17	23.8	2.9e-17	23.8
64.7	1.3e-15	26.8	1.3e-15	26.8	1.3e-15	26.8
75.6	2.5e-14	28.7	2.5e-14	28.7	2.5e-14	28.7
85.1	8.0e-14	29.1	8.0e-14	29.1	8.0e-14	29.2

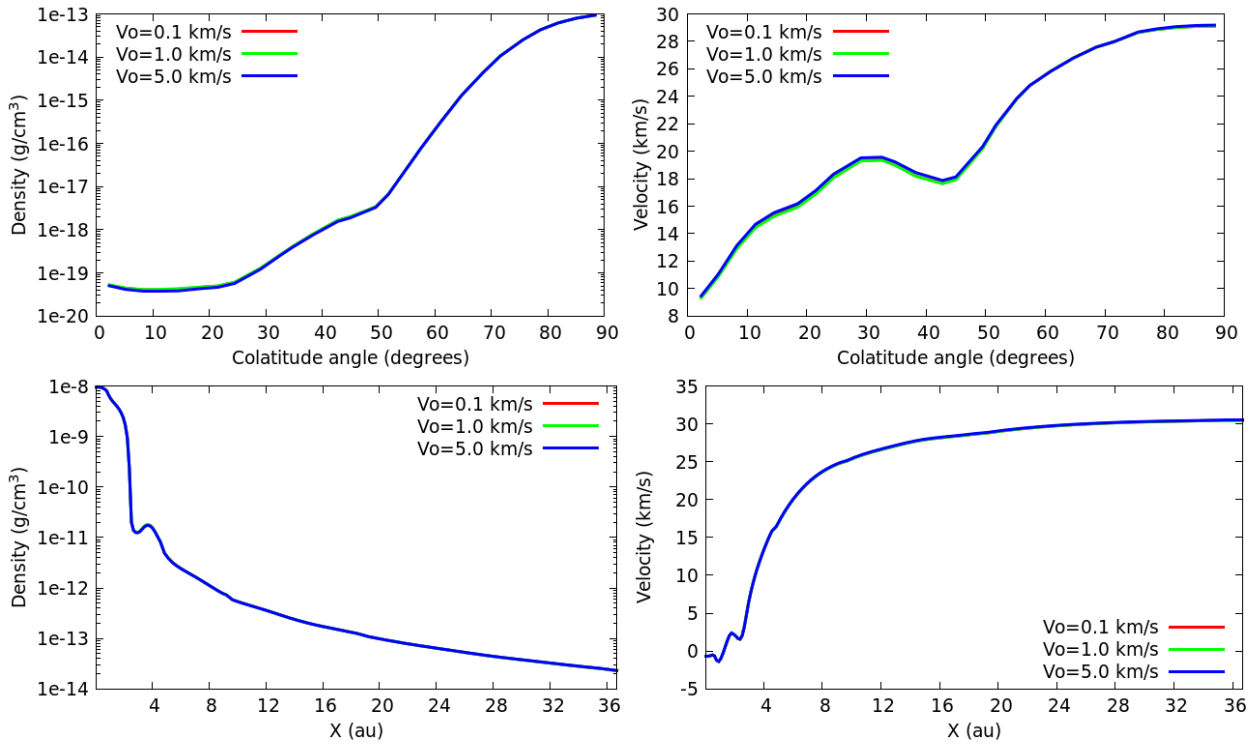

Figure 3.13 Top row: time-averaged colatitudinal profiles of density (left) and outflow velocity (right) at 20.0 au from the barycentre. **Bottom row**: time-averaged radial profiles of density (left) and outflow velocity (right) at the orbital plane. At the onset of simulations, the wind velocity (Vo) at the surface of the AGB star is different for each Model.

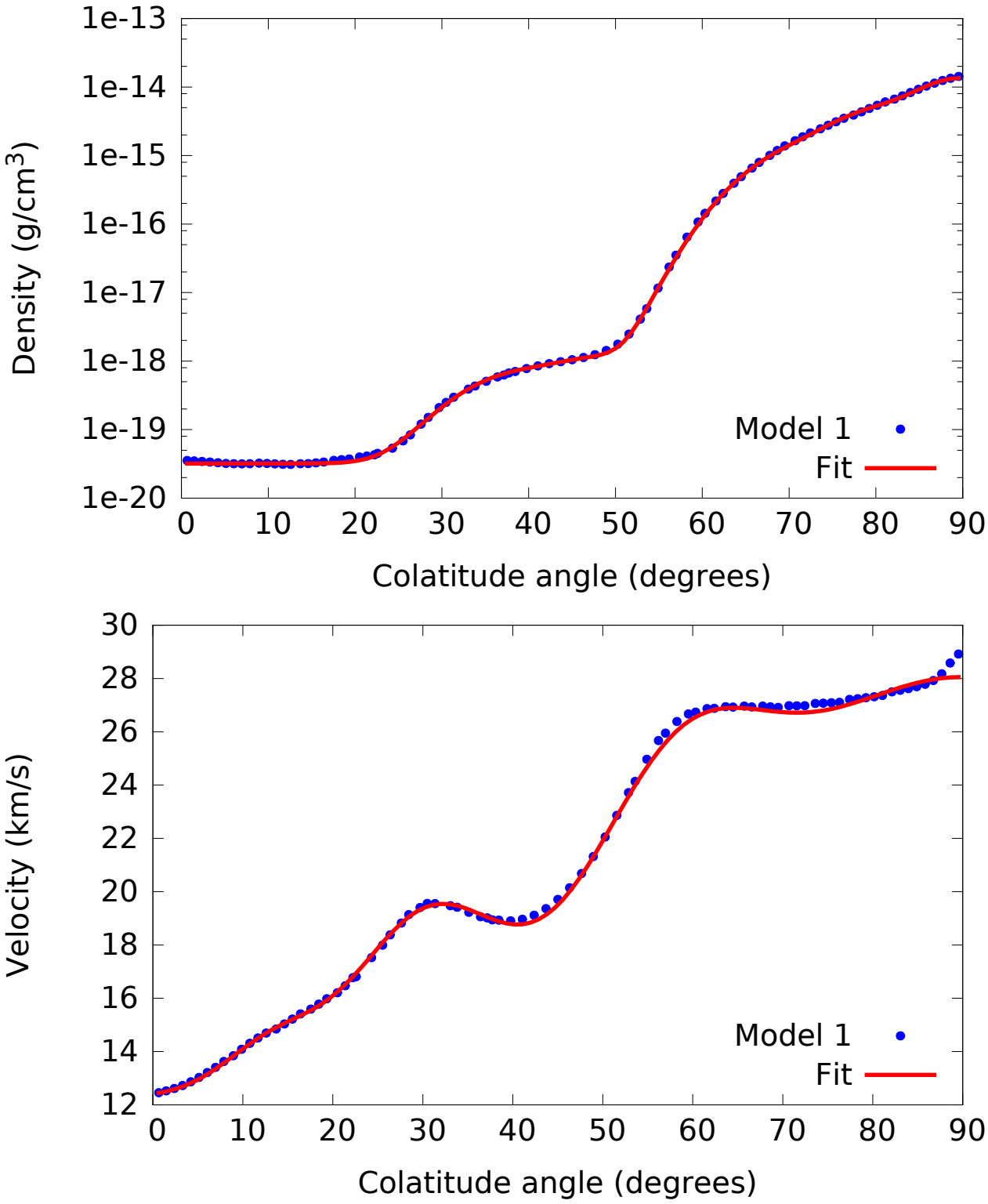

Figure 3.14 Time-averaged density (top) and outflow velocity (bottom) profiles, as functions of the colatitude angle, at 20.0 au from the barycentre of the system for our fiducial model (• symbols). Solid lines are analytical fits from equations (3.1) and (3.2).

Chapter Four

Discussion

One of the most important feature from the above results is that the outflow has a complex non-spherical structure. Our results show that the time-averaged density is maximal at the orbital plane and minimal along the poles. Thus for example, the interactions of an ejected CE will be affected by this gas distribution, even more the subsequent PNe formation (García-Segura, Ricker, and Taam, 2018). This suggests that the connection between PNe symmetry axis and binary star parameters (Jones et al., 2012) is established before RLOF and survives the CE phase.

The pole-to-equator density ratio is also important in the shaping of a hot bubble resulting from the shocked material by a jet from the secondary star, at the RLOF phase (Shiber et al., 2019, and references therein). For the above reasons, the density ratio has to be taken into account to study the correct hydrodynamical evolution of the binary system.

For a single AGB star with pulsation period $P = 300$ days, parametrizations for mass-loss rates from Vassiliadis and Wood (1993) and De Beck et al. (2010) agree within one order of magnitude with the mass-loss rate of Model 3, where the binary star has its largest orbital separation and the companion star has the lowest influence. For the other models, the mass-loss rates are larger and comparable to those in AGB stars undergoing superwinds (Renzini, 1981; Vassiliadis and Wood, 1993).

There are three implications for the above result. First, the AGB timescale could be shortened if such mass-loss rates are maintained or enhanced by the CE (see e.g. De Marco et al., 2011). Second, superwinds at the tip of the AGB phase could be actually gravity-enhanced winds in binary systems approaching RLOF (see e.g. Decin et al., 2019). Third, the stellar evolution of the primary could be driven by the presence of a companion star rather than by intrinsic properties (see e.g. Sana et al., 2012). This can reduce the final mass of white dwarfs in binary systems.

The total mass of the wind leaving the computational domain through the outer boundaries can be calculated multiplying the time-averaged mass-loss rate (Table 3.2) by the total computational time (40 orbital periods). From this, it is obtained for Models 1, 2, 3, 4, 5, 6 and 7 a total mass loss of 7.4×10^{-3} $M_\odot$, 2.7×10^{-4} $M_\odot$, 2.5×10^{-5} $M_\odot$, 8.3×10^{-4} $M_\odot$, 2.3×10^{-3} $M_\odot$, 5.6×10^{-3} $M_\odot$ and 1.3×10^{-1} $M_\odot$, respectively. Thus, despite the large rates of mass loss found in our Models, the total mass of the outflow leaving the computational domain is several orders of magnitude smaller than the mass of the binary stars, which justifies why the self-gravity of the outflow is neglected. An exception to the above can be Model 7, where the total mass loss is ~ 6 per cent of the primary stellar mass M_1; however, it has long been recognised that adiabatic models of AGB atmospheres overestimate the outflows mass-loss rate (Wood, 1979; Bowen, 1988).

Dynamical interactions between circumbinary disks and binary stars are considered by Artymowicz et al. (1991) and Dermine et al. (2013) as a mechanism to increase the orbit eccentricity. However our models show that there is no gravitationally-bounded circumbinary disks when radiation pressure on dust is taken into account. This implies that the above-mentioned mechanism may not work for AGB binaries with dusty winds and approaching RLOF. Our models also suggest that such disks observed in post-AGB binaries (Van Winckel et al., 2006) must be formed after RLOF or when the dust-driven wind is over.

The accretion disk around the main-sequence companion and the Roche lobe of the latter has approximately the same radius (Paczynski, 1977). Using equation (2.9) with the stellar mass ratio $q = M_2/M_1 = 0.8\ M_\odot/2.2\ M_\odot$ and $a = 674.3$ $R_\odot$, the Roche lobe radius for the secondary star is ~ 200 $R_\odot$, which is ~ 11 times the size of a mesh cell. At this distance the smoothed gravitational potential (equation 2.20) is identical to the Newtonian potential, and mass loss through the Lagrangian point L_2 is unaffected by the parameter $\varepsilon = 3$. In addition, our simulations of binary systems with the same orbital separation but more massive secondary stars (with a deeper gravitational potential well) show that the outflow structure is well described by the same formulae. Therefore we expect that our qualitative results remain valid, even though the accretion disk physics is not resolved.

The size of the grid (~ 20 au from the centre of mass to the free-outflow boundaries) was chosen taking into account the computational cost of the numerical models for a given maximum resolution. For instance, doubling the resolution would cost $\sim 2^4$ times (twice for every Cartesian coordinate and the fact that the time step is reduce by half) more computing time for the same numerical model. In

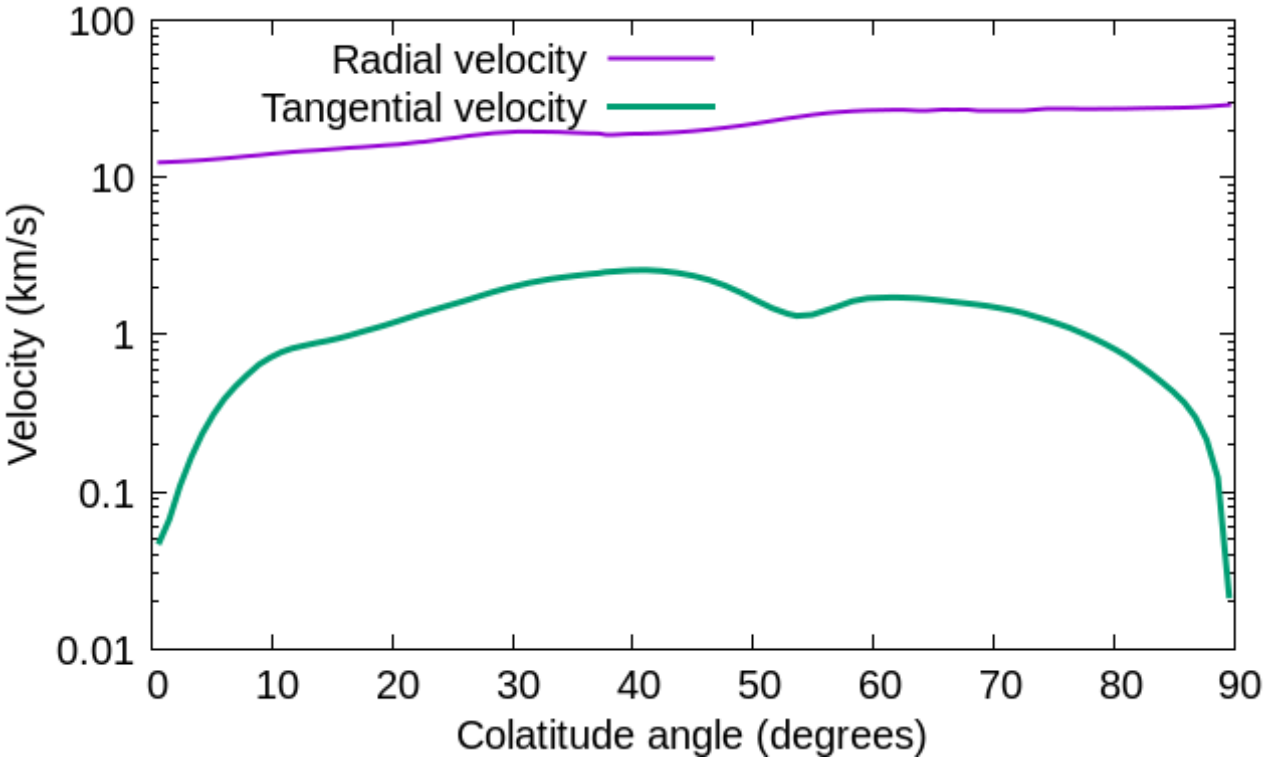

Figure 4.1 Time-averaged radial and tangential velocity for Model 1. The latter velocity was multiplied by minus one to plot it in logarithmic scale.

consequence the Model 1, whose total computing time was five days and fourteen hours at a maximum resolution of $\sim 35.2\ R_{\odot}$, would cost approximately three months to complete at twice the resolution. This is a prohibitive amount of time for each Model, specially if several models are required. With that in mind, one is forced to ask oneself if the wind has reached an asymptotic structure at a distance of 20 au from the centre of mass of the binary system. If that is the case, the tangential velocities should be smaller in magnitude compared to the radial velocity. These two velocities are shown in Figure 4.1, where it can be seen that the tangential velocity is at most 10 per cent as large as the radial velocity. Although not a rigorous proof, this figure may help to explain why a larger numerical domain is not the most pressing need.

Our models show outflows with pole-to-equator density ratios from 10^2 up to $\sim 10^5$. On the one hand, such high ratios are consistent with those between the polar wind density and the density of a disk formed through the wind-compressed disk (WCD) model (Bjorkman and Cassinelli, 1993; Ignace, Cassinelli, and Bjorkman, 1996). It is note worthy to indicate that the validity of the WCD model to AGB stars in binary systems is uncertain (García-Segura, Villaver, Manchado, et al., 2016). On the other hand, hydrodynamic simulations (Icke, Preston, and Balick, 1989; Mellema, Eulderink, and Icke, 1991; Icke, 1991; Icke, Balick, and Frank, 1992; Frank and Mellema, 1994; Dwarkadas,

Chevalier, and Blondin, 1996) show the formation of PNe with either bipolar lobes or collimated bubbles when the density contrast of the AGB slow wind is larger than about $\sim 5-10$. These values are one to four order of magnitudes smaller than that obtained in the Models of the chapter three. However, the grid spatial scale in the above mentioned simulations is two orders of magnitude larger. Thus, it is possible that during the time in which the axisymmetric AGB wind expands to the characteristic length scales of proto-PNe, the tangential motions due to pressure gradients reduce the density contrast to the values employed in previous studies. Finally, we note that the pole-to-equator density ratio is reduced if radiative cooling is absent. This implies that a complete computation of PNe formation and evolution must include a self-consistent treatment of radiative cooling.

The time-averaged structure of the outflows from our interacting binary stars is well described using the proposed analytical formulae. Motivated by the fact that our models include both semi-detached and detached binaries, future work will explore if our formulae remain valid for a much larger combination of orbital separations and stellar mass ratios.

Chapter Five

Conclusions

We have computed numerically the outflow from interacting binary stars. The results of our study can be summarized as follows: mass loss from an interacting binary system hosting an AGB star is produced mainly through the outer Lagrangian points, as shown also in Soker and Livio (1989), Mastrodemos and Morris (1999), and Mohamed and Podsiadlowski (2007).

The resultant pole-to-equator density ratios and mass-loss rates increase in binary systems with smaller orbital separations or with larger mass ratios $q = M_2/M_1$ (top panels of Figures 3.4 and 3.6). At the RLOF phase, both density ratio and mass-loss rate have the largest values.

These results agree with the hypothesis of binary stars as a shaping mechanisms of aspherical PNe.

If radiation pressure on dust grains is included, the gas leaving the Lagrangian L_2 point does not establish an outer ring of gravitationally bound matter when $q = M_2/M_1 > 0.78$. This behaviour is the opposite when radiation pressure is not included (Shu, Lubow, and Anderson, 1979; Pejcha, Metzger, and Tomida, 2016; Chen et al., 2017).

We find analytical formulae describing the outflow structure in terms of distance from the barycentre and the colatitude angle. The formulae can be used in future studies to setup hydrodynamic simulations of CE evolution and the formation of planetary nebulae.

APPENDIX

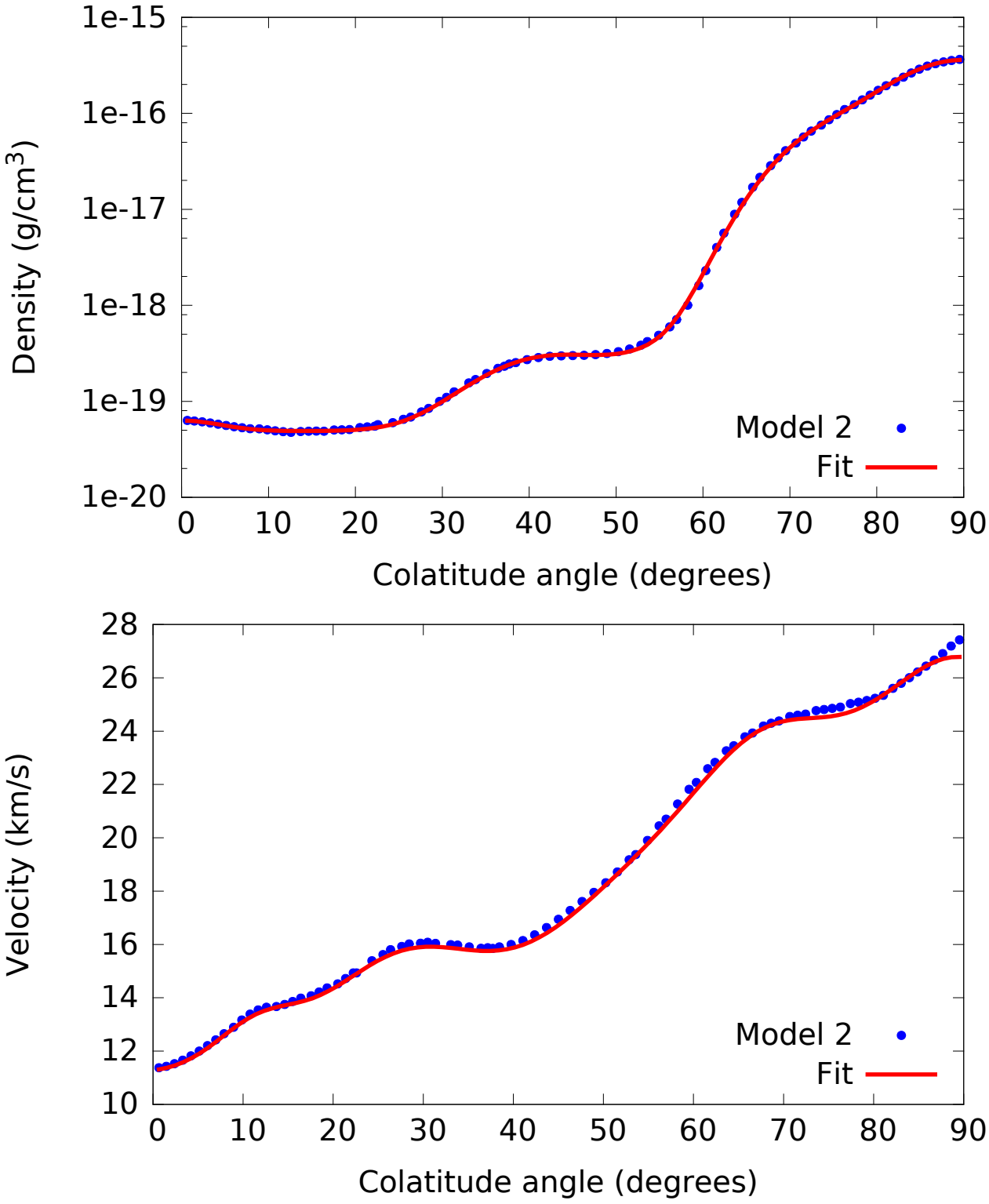

Figure 1 Same as Fig. 3.14 for model 2.

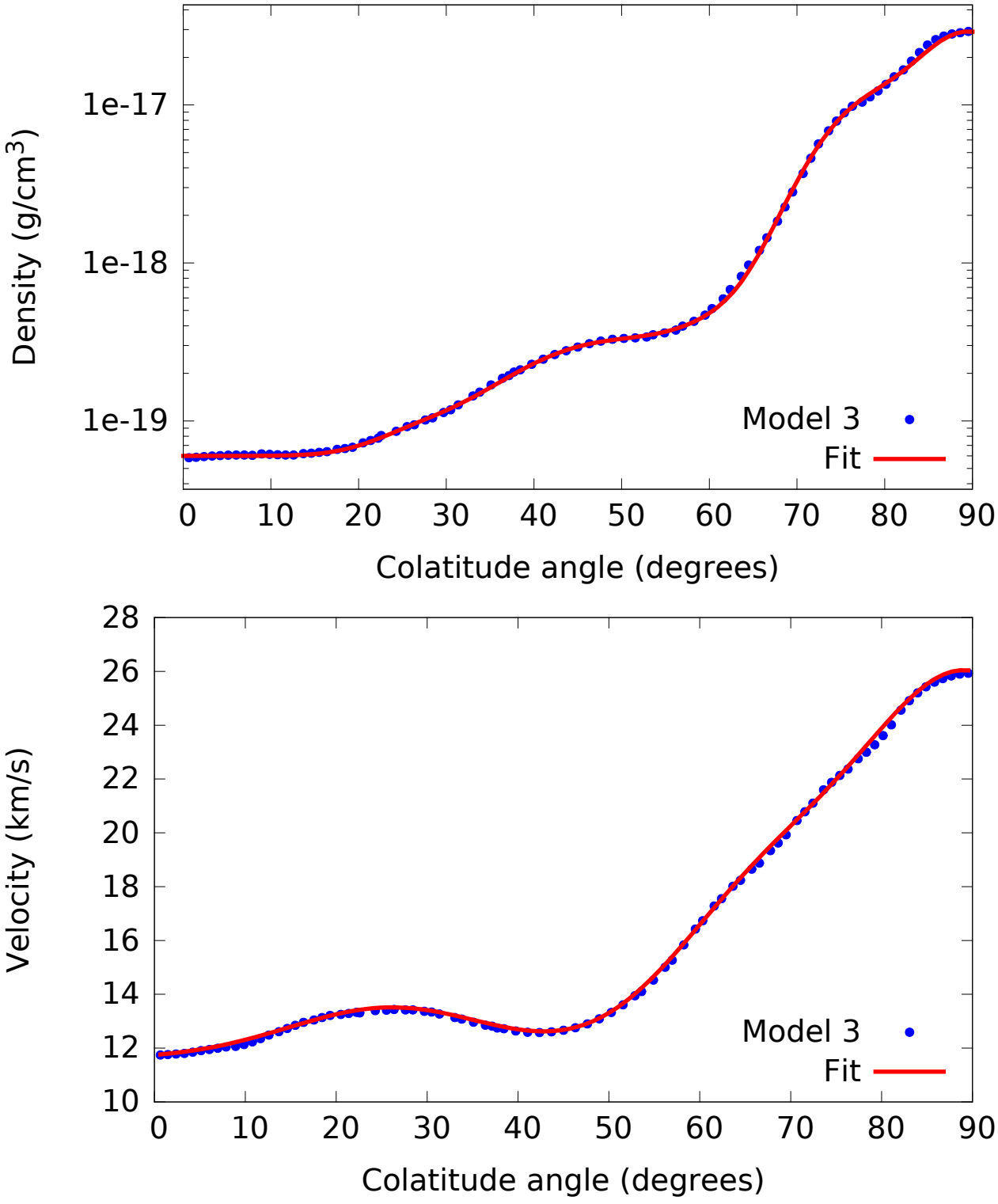

Figure 2 Same as Fig. 3.14 for model 3.

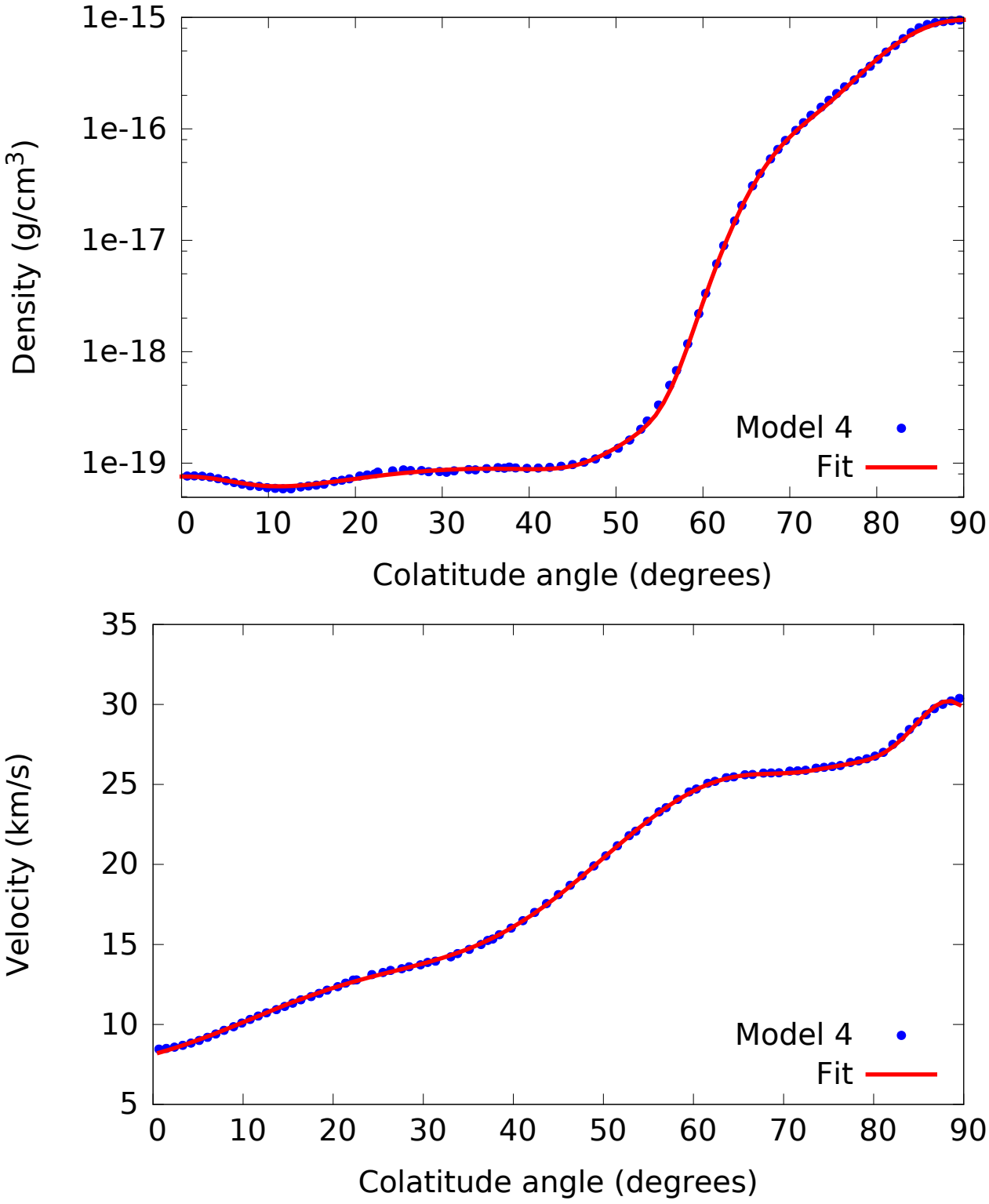

Figure 3 Same as Fig. 3.14 for model 4.

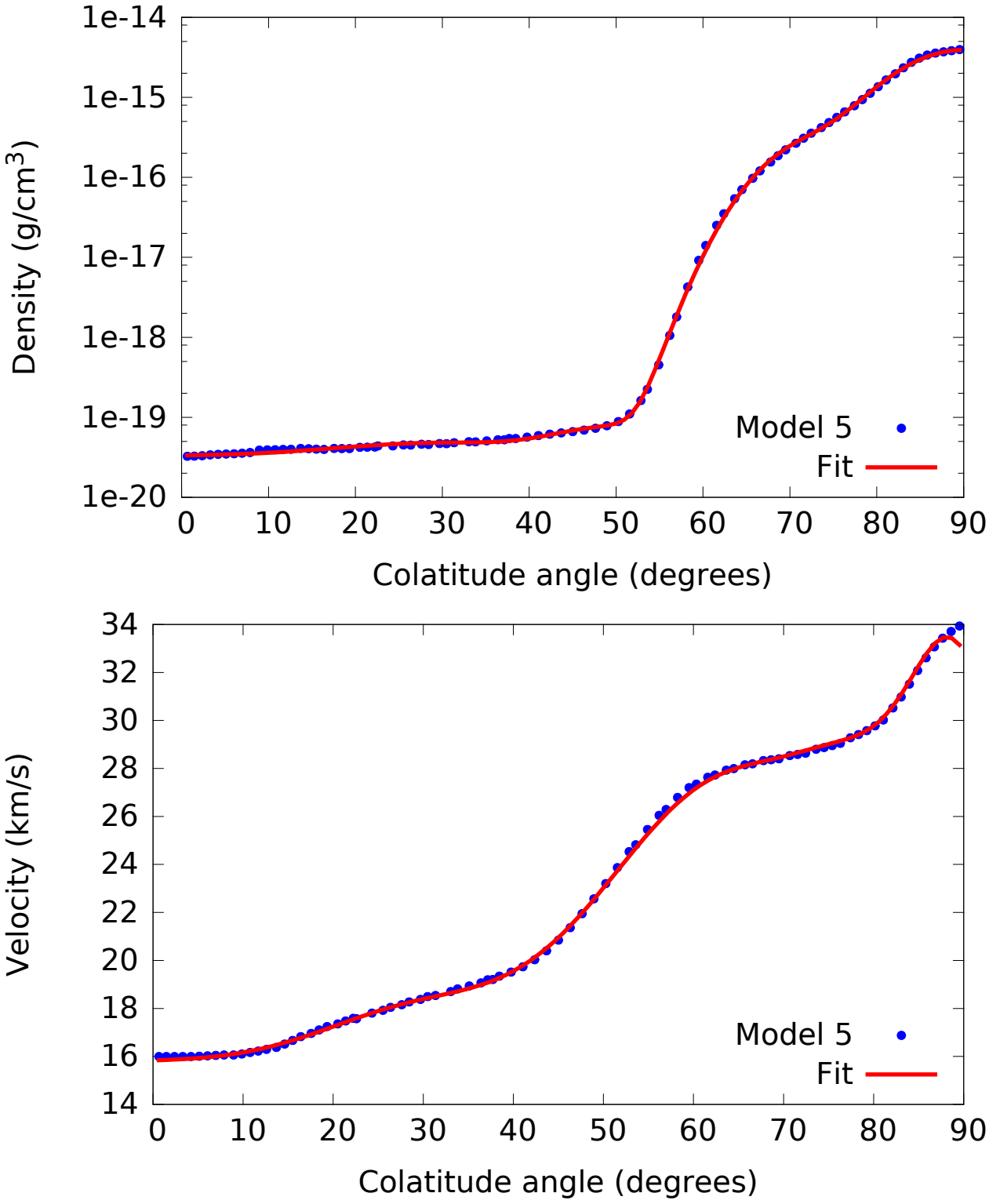

Figure 4 Same as Fig. 3.14 for model 5.

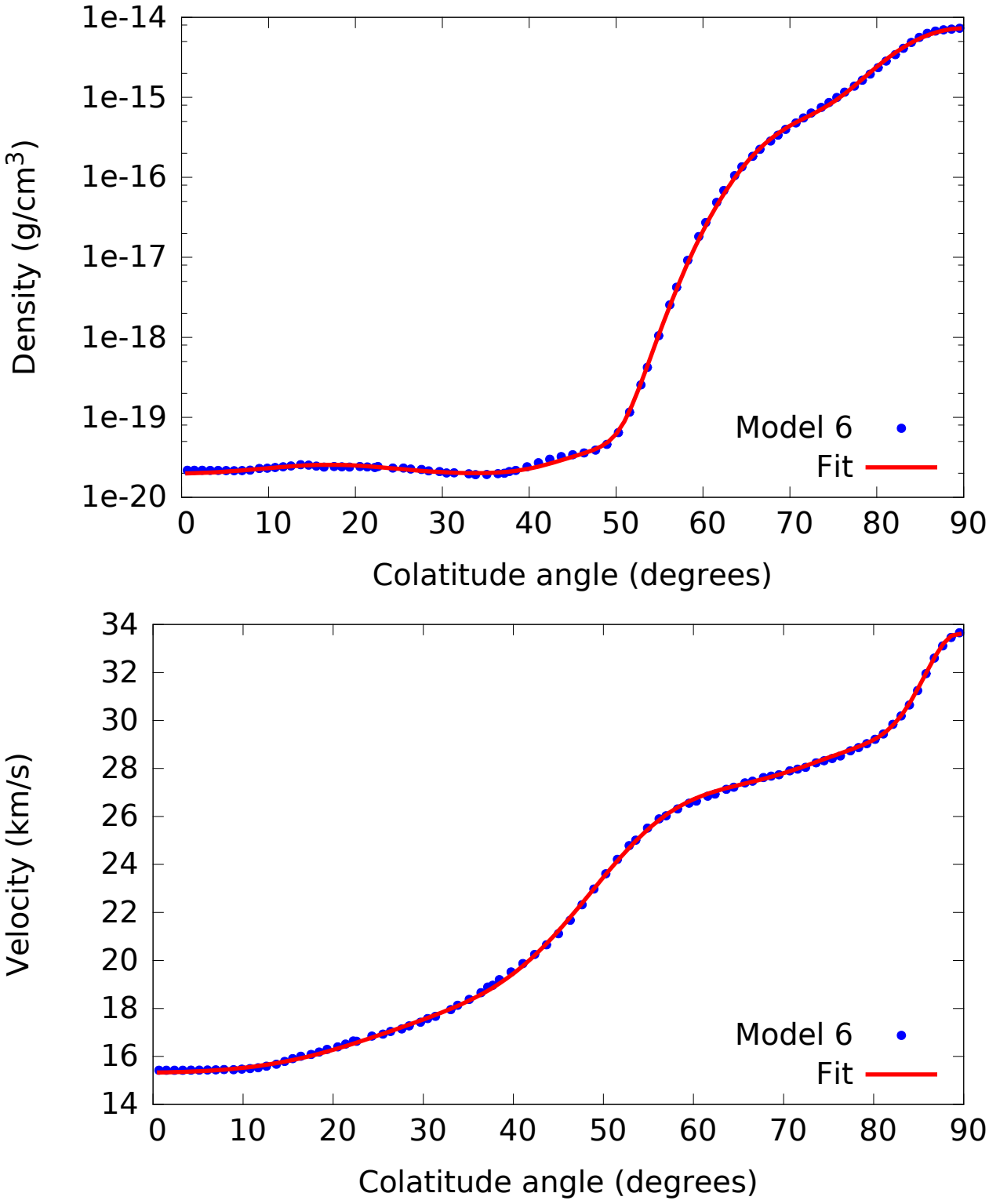

Figure 5 Same as Fig. 3.14 for model 6.

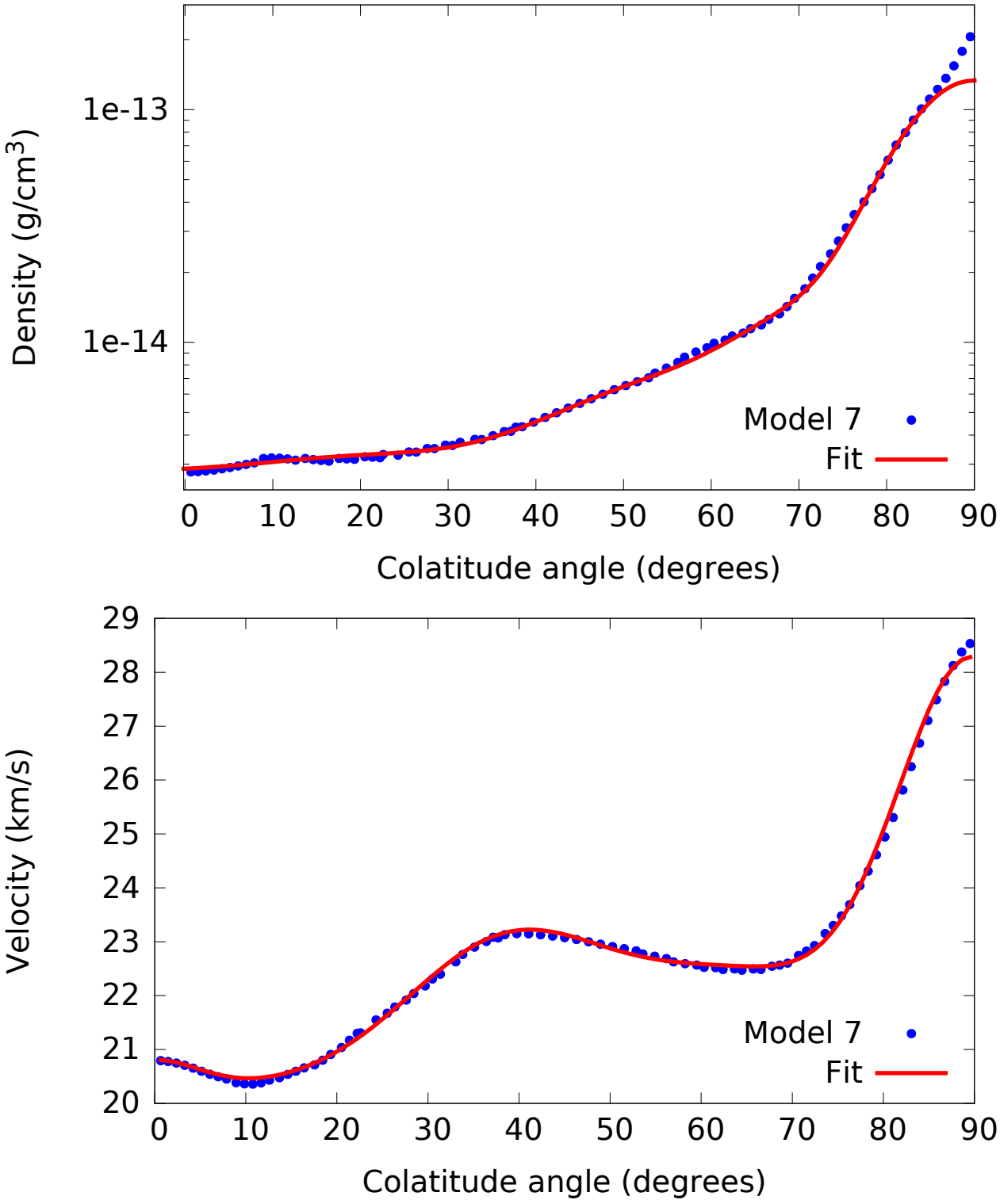

Figure 6 Same as Fig. 3.14 for model 7.

REFERENCES

Alcolea et al. (July 2001). "The highly collimated bipolar outflow of OH 231.8+4.2". In: *A&A* 373, pp. 932–949. DOI: 10.1051/0004-6361:20010535.

Applegate (June 1988). "Why stars become red giants". In: *ApJ* 329, pp. 803–807. DOI: 10.1086/166423.

Artymowicz et al. (Mar. 1991). "The Effect of an External Disk on the Orbital Elements of a Central Binary". In: *ApJ* 370, p. L35. DOI: 10.1086/185971.

Asida and Tuchman (Dec. 1995). "Asymmetrical Mass Loss from Rotating Red Giant Variables". In: *ApJ* 455, p. 286. DOI: 10.1086/176576.

Balick (Sept. 1987). "The evolution of planetary nebulae. I - Structures, ionizations, and morphological sequences". In: *AJ* 94, pp. 671–678. DOI: 10.1086/114504.

Berlioz-Arthaud (Jan. 2003). "Mira Variables explained by a planetary companion interaction: A means to drop the pulsation paradigm?" In: *A&A* 397, pp. 943–950. DOI: 10.1051/0004-6361:20021540.

Binnendijk (Jan. 1965). "The W Ursae Majoris Systems". In: *Veroeffentlichungen der Remeis-Sternwarte zu Bamberg* 27.40, p. 36.

Bjorkman and Cassinelli (May 1993). "Equatorial Disk Formation around Rotating Stars Due to Ram Pressure Confinement by the Stellar Wind". In: *ApJ* 409, p. 429. DOI: 10.1086/172676.

Black (Nov. 1981). "The physical state of primordial intergalactic clouds". In: *MNRAS* 197, pp. 553–563. DOI: 10.1093/mnras/197.3.553.

Blackman (July 2004). "Dynamo-Driven Outflows in Pre-Planetary Nebulae". In: *Asymmetrical Planetary Nebulae III: Winds, Structure and the Thunderbird*. Ed. by Margaret Meixner et al. Vol. 313. Astronomical Society of the Pacific Conference Series, p. 401. arXiv: astro-ph/0309752 [astro-ph].

Bodenheimer et al. (Jan. 2007). "Numerical Methods in Astrophysics: An Introduction". In: *Numerical Methods in Astrophysics: An Introduction. Part of the Series in Astronomy and Astrophysics. Edited by Peter Bodenheimer.*

Bond and Livio (June 1990). "Morphologies of Planetary Nebulae Ejected by Close-Binary Nuclei". In: *ApJ* 355, p. 568. DOI: 10.1086/168789.

Bowen (June 1988). "Dynamical modeling of long-period variable star atmospheres". In: *ApJ* 329, pp. 299–317. DOI: 10.1086/166378.

Bujarrabal et al. (Sept. 2013). "Extended rotating disks around post-AGB stars". In: *A&A* 557, A104, A104. DOI: 10.1051/0004-6361/201322015. arXiv: 1307.1975 [astro-ph.GA].

Carpenter et al. (Dec. 2018). "The Advanced Spectral Library (ASTRAL): Reference Spectra for Evolved M Stars". In: *ApJ* 869.2, 157, p. 157. DOI: 10.3847/1538-4357/aaf164. arXiv: 1811.11865 [astro-ph.SR].

Chamandy, Frank, et al. (2018). "Accretion in common envelope evolution". In: *MNRAS* 480, pp. 1898–1911. DOI: 10.1093/mnras/sty1950. arXiv: 1805.03607 [astro-ph.SR].

Chamandy, Tu, et al. (June 2019). "Energy budget and core-envelope motion in common envelope evolution". In: *MNRAS* 486.1, pp. 1070–1085. DOI: 10.1093/mnras/stz887. arXiv: 1812.11196 [astro-ph.SR].

Chandrasekhar (1967). *An introduction to the study of stellar structure*.

Chen et al. (July 2017). "Mass transfer and disc formation in AGB binary systems". In: *MNRAS* 468.4, pp. 4465–4477. DOI: 10.1093/mnras/stx680. arXiv: 1702.06160 [astro-ph.SR].

Chevalier and Luo (Jan. 1994). "Magnetic Shaping of Planetary Nebulae and Other Stellar Wind Bubbles". In: *ApJ* 421, p. 225. DOI: 10.1086/173640.

Chibueze et al. (Feb. 2016). "Near-infrared Observations of SiO Maser-emitting Asymptotic Giant Branch (AGB) Stars". In: *ApJ* 817.2, 115, p. 115. DOI: 10.3847/0004-637X/817/2/115.

Childs, Hank et al. (Oct. 2012). "VisIt: An End-User Tool For Visualizing and Analyzing Very Large Data". In: *High Performance Visualization–Enabling Extreme-Scale Scientific Insight*, pp. 357–372.

Corradi, Brandi, et al. (Mar. 1999). "A narrowband imaging survey of symbiotic stars". In: *A&A* 343, pp. 841–846.

Corradi and Schwarz (Jan. 1995). "Morphological populations of planetary nebulae: which progenitors? I. Comparative properties of bipolar nebulae." In: *A&A* 293, pp. 871–888.

Danilovich et al. (Sept. 2015). "New observations and models of circumstellar CO line emission of AGB stars in the Herschel SUCCESS programme". In: *A&A* 581, A60, A60. DOI: 10.1051/0004-6361/201526705. arXiv: 1506.09065 [astro-ph.SR].

De Beck et al. (Nov. 2010). "Probing the mass-loss history of AGB and red supergiant stars from CO rotational line profiles. II. CO line survey of evolved stars: derivation of mass-loss rate formulae". In: *A&A* 523, A18, A18. DOI: 10.1051/0004-6361/200913771. arXiv: 1008.1083 [astro-ph.SR].

De Marco (Apr. 2009). "The Origin and Shaping of Planetary Nebulae: Putting the Binary Hypothesis to the Test". In: *PASP* 121.878, p. 316. DOI: 10.1086/597765. arXiv: 0902.1137 [astro-ph.GA].

De Marco et al. (Mar. 2011). "On the α formalism for the common envelope interaction". In: *MNRAS* 411.4, pp. 2277–2292. DOI: 10.1111/j.1365-2966.2010.17891.x. arXiv: 1010.4374 [astro-ph.SR].

de Val-Borro, Karovska, and Sasselov (Aug. 2009). "Numerical Simulations of Wind Accretion in Symbiotic Binaries". In: *ApJ* 700.2, pp. 1148–1160. DOI: 10.1088/0004-637X/700/2/1148. arXiv: 0905.3542 [astro-ph.SR].

Decin et al. (Feb. 2019). "Reduction of the maximum mass-loss rate of OH/IR stars due to unnoticed binary interaction". In: *Nature Astronomy* 3, pp. 408–415. DOI: 10.1038/s41550-019-0703-5. arXiv: 1902.09259 [astro-ph.SR].

Dermine et al. (Mar. 2013). "Eccentricity-pumping in post-AGB stars with circumbinary discs". In: *A&A* 551, A50, A50. DOI: 10.1051/0004-6361/201219430.

Djurasevic (July 1986). "Critical equipotential surfaces in close binary systems". In: *Ap&SS* 124, pp. 5–25. DOI: 10.1007/BF00649745.

Doan et al. (Jan. 2020). "The extended molecular envelope of the asymptotic giant branch star π^1 Gruis as seen by ALMA. II. The spiral-outflow observed at high-angular resolution". In: *A&A* 633, A13, A13. DOI: 10.1051/0004-6361/201935245. arXiv: 1911.10756 [astro-ph.SR].

Dwarkadas, Chevalier, and Blondin (Feb. 1996). "The Shaping of Planetary Nebulae: Asymmetry in the External Wind". In: *ApJ* 457, p. 773. DOI: 10.1086/176772.

Eggleton (May 1983). "Approximations to the radii of Roche lobes". In: *ApJ* 268, p. 368. DOI: 10.1086/160960.

Esquivel et al. (Dec. 2010). "A Model of Mira's Cometary Head/Tail Entering the Local Bubble". In: *ApJ* 725, pp. 1466–1475. DOI: 10.1088/0004-637X/725/2/1466. arXiv: 1010.3167.

Fadeyev (Oct. 2016). "Nonlinear pulsations of stars with initial mass $3M_\odot$ on the asymptotic giant branch". In: *Astronomy Letters* 42.10, pp. 665–673. DOI: 10.1134/S1063773716090024. arXiv: 1605.03851 [astro-ph.SR].

Frank and Mellema (Aug. 1994). "The Radiation Gasdynamics of Planetary Nebulae. IV. From the Owl to the Eskimo". In: *ApJ* 430, p. 800. DOI: 10.1086/174450. arXiv: astro-ph/9404077 [astro-ph].

Fuhrmann et al. (Feb. 2017). "Multiplicity among Solar-type Stars". In: *ApJ* 836.1, 139, p. 139. DOI: 10.3847/1538-4357/836/1/139.

Gail and Sedlmayr (Dec. 2013). *Physics and Chemistry of Circumstellar Dust Shells*.

García-Segura, Langer, et al. (June 1999). "Shaping Bipolar and Elliptical Planetary Nebulae: Effects of Stellar Rotation, Photoionization Heating, and Magnetic Fields". In: *ApJ* 517, pp. 767–781. DOI: 10.1086/307205.

García-Segura, Ricker, and Taam (June 2018). "Common Envelope Shaping of Planetary Nebulae". In: *ApJ* 860, 19, p. 19. DOI: 10.3847/1538-4357/aac08c. arXiv: 1804.09309 [astro-ph.SR].

García-Segura, Villaver, Langer, et al. (Mar. 2014). "Single Rotating Stars and the Formation of Bipolar Planetary Nebula". In: *ApJ* 783, 74, p. 74. DOI: 10.1088/0004-637X/783/2/74. arXiv: 1401.4414 [astro-ph.SR].

García-Segura, Villaver, Manchado, et al. (June 2016). "Rotating Stars and the Formation of Bipolar Planetary Nebulae. II. Tidal Spin-up". In: *ApJ* 823, 142, p. 142. DOI: 10.3847/0004-637X/823/2/142. arXiv: 1604.01671 [astro-ph.SR].

Gawryszczak, Mikołajewska, and Różyczka (Apr. 2002). "Morphology of planetary nebulae with binary cores. The effect of gravitational focusing by the companion to the mass-losing star". In: *A&A* 385, pp. 205–215. DOI: 10.1051/0004-6361:20011800.

Gullikson, Kraus, and Dodson-Robinson (Aug. 2016). "The Close Companion Mass-ratio Distribution of Intermediate-mass Stars". In: *AJ* 152, 40, p. 40. DOI: 10.3847/0004-6256/152/2/40. arXiv: 1604.06456 [astro-ph.SR].

Habing and Olofsson (2004). *Asymptotic Giant Branch Stars*. DOI: 10.1007/978-1-4757-3876-6.

Hairer, Lubich, and Wanner (Jan. 2003). "Geometric numerical integration illustrated by the Störmer-Verlet method". In: *Acta Numerica* 12, pp. 399–450. DOI: 10.1017/S0962492902000144.

Hansen, Kawaler, and Trimble (2004). *Stellar interiors : physical principles, structure, and evolution*.

Hernández et al. (Apr. 2014). "A Hydrodynamical Mechanism for Generating Astrophysical Jets". In: *Rev. Mex. Astron. Astrofis.* 50, pp. 23–35. arXiv: 1103.0250 [astro-ph.HE].

Hillwig et al. (Dec. 2016). "Observational Confirmation of a Link Between Common Envelope Binary Interaction and Planetary Nebula Shaping". In: *ApJ* 832, 125, p. 125. DOI: 10.3847/0004-637X/832/2/125. arXiv: 1609.02185 [astro-ph.SR].

Höfner and Olofsson (Jan. 2018). "Mass loss of stars on the asymptotic giant branch. Mechanisms, models and measurements". In: *A&ARv* 26.1, 1, p. 1. DOI: 10.1007/s00159-017-0106-5.

Holzer and MacGregor (July 1985). "Mass Loss Mechanisms for Cool, Low-Gravity Stars (Review)". In: *Mass Loss from Red Giants*. Ed. by M. Morris and B. Zuckerman. Vol. 117, p. 229. DOI: 10.1007/978-94-009-5428-1_21.

Homan et al. (Aug. 2018). "An unusual face-on spiral in the wind of the M-type AGB star EP Aquarii". In: *A&A* 616, A34, A34. DOI: 10.1051/0004-6361/201832834. arXiv: 1804.05684 [astro-ph.SR].

Huarte-Espinosa et al. (Aug. 2012). "From bipolar to elliptical: simulating the morphological evolution of planetary nebulae". In: *MNRAS* 424, pp. 2055–2068. DOI: 10.1111/j.1365-2966.2012.21348.x. arXiv: 1107.0415 [astro-ph.SR].

Iben (2013). *Stellar Evolution Physics, Volume 1: Physical Processes in Stellar Interiors*.

Icke (Nov. 1991). "The hydrodynamics of aspherical planetary nebulae. I - Analytic evaluation of hydrodynamic difference schemes". In: *A&A* 251.1, pp. 369–381.

Icke, Balick, and Frank (Jan. 1992). "The hydrodynamics of aspherical planetary nebulae. II - Numerical modelling of the early evolution". In: *A&A* 253, pp. 224–243.

Icke, Preston, and Balick (Feb. 1989). "The evolution of planetary nebulae. III - Position-velocity images of butterfly-type nebulae". In: *AJ* 97, pp. 462–475. DOI: 10.1086/114995.

Ignace, Cassinelli, and Bjorkman (Mar. 1996). "Equatorial Wind Compression Effects across the H-R Diagram". In: *ApJ* 459, p. 671. DOI: 10.1086/176932.

Ivanova, Justham, Chen, et al. (Feb. 2013). "Common envelope evolution: where we stand and how we can move forward". In: *A&ARv* 21, 59, p. 59. DOI: 10.1007/s00159-013-0059-2. arXiv: 1209.4302 [astro-ph.HE].

Ivanova, Justham, and Podsiadlowski (Mar. 2015). "On the role of recombination in common-envelope ejections". In: *MNRAS* 447.3, pp. 2181–2197. DOI: 10.1093/mnras/stu2582. arXiv: 1409.3260 [astro-ph.SR].

Jones et al. (Mar. 2012). "The morphology and kinematics of the Fine Ring Nebula, planetary nebula Sp 1, and the shaping influence of its binary central star". In: *MNRAS* 420, pp. 2271–2279. DOI: 10.1111/j.1365-2966.2011.20192.x. arXiv: 1111.2860 [astro-ph.SR].

Kahn and Breitschwerdt (Feb. 1990). "Dynamical evolution of planetary nebulae. I - Formation of shells in an accelerating wind in protoplanetary nebulae". In: *MNRAS* 242, pp. 505–511. DOI: 10.1093/mnras/242.3.505.

Kahn and West (Feb. 1985). "Shapes of planetary nebulae". In: *MNRAS* 212, pp. 837–850. DOI: 10.1093/mnras/212.4.837.

Kastner and Weintraub (Mar. 1995). "Near-Infrared Polarimetric Imaging of the Bipolar Mebula OH 231.8+4.2: The Death of a Beta Pic-Like System?" In: *AJ* 109, p. 1211. DOI: 10.1086/117354.

Khouri et al. (Oct. 2014). "The wind of W Hydrae as seen by Herschel. II. The molecular envelope of W Hydrae". In: *A&A* 570, A67, A67. DOI: 10.1051/0004-6361/201424298. arXiv: 1409.0396 [astro-ph.SR].

Kopal (1959). *Close binary systems*.

Kwok (2002). "Interacting Stellar Winds and the Shaping of Planetary Nebulae". In: *Interacting Winds from Massive Stars*. Ed. by A.F.J. Moffat and N. St-Louis. Vol. 260. Astronomical Society of the Pacific Conference Series, p. 245.

Kwok, Purton, and Fitzgerald (Feb. 1978). "On the origin of planetary nebulae". In: *ApJ* 219, pp. L125–L127. DOI: 10.1086/182621.

Lamers and Cassinelli (June 1999). *Introduction to Stellar Winds*, p. 452.

Lebzelter and Hinkle (Jan. 2002). "Periodic and Nonperiodic Phenomena in AGB Stars". In: *IAU Colloq. 185: Radial and Nonradial Pulsationsn as Probes of Stellar Physics*. Ed. by Conny Aerts, Timothy R. Bedding, and Jørgen Christensen-Dalsgaard. Vol. 259. Astronomical Society of the Pacific Conference Series, p. 556. arXiv: astro-ph/0202476 [astro-ph].

Leisenring, Kemper, and Sloan (July 2008). "Effects of Metallicity on the Chemical Composition of Carbon Stars". In: *ApJ* 681.2, pp. 1557–1573. DOI: 10.1086/588378. arXiv: 0803.3067 [astro-ph].

Livio (Jan. 1995). "The Formation of Axisymmetric Nebulae". In: *Asymmetrical Planetary Nebulae*. Ed. by A. Harpaz and N. Soker. Vol. 11, p. 51.

Lodders and Fegley (Nov. 1995). "The origin of circumstellar silicon carbide grains found in meteorites". In: *Meteoritics* 30.6, p. 661. DOI: 10.1111/j.1945-5100.1995.tb01164.x.

Loup, C. et al. (June 1993). "CO and HCN observations of circumstellar envelopes. A catalogue - mass loss rates and distributions." In: *A&AS* 99, pp. 291–377.

Maercker et al. (Oct. 2012). "Unexpectedly large mass loss during the thermal pulse cycle of the red giant star R Sculptoris". In: *Nature* 490.7419, pp. 232–234. DOI: 10.1038/nature11511. arXiv: 1210.3030 [astro-ph.SR].

Manchado (July 2004). "Correlation of PN Morphologies and Nebular Parameters". In: *Asymmetrical Planetary Nebulae III: Winds, Structure and the Thunderbird*. Ed. by Margaret Meixner et al. Vol. 313. Astronomical Society of the Pacific Conference Series, p. 3.

Manchado et al. (1996). *The IAC morphological catalog of northern Galactic planetary nebulae*.

Mastrodemos and Morris (Sept. 1999). "Bipolar Pre-Planetary Nebulae: Hydrodynamics of Dusty Winds in Binary Systems. II. Morphology of the Circumstellar Envelopes". In: *ApJ* 523, pp. 357–380. DOI: 10.1086/307717.

McDonald et al. (Dec. 2018). "Pulsation-triggered dust production by asymptotic giant branch stars". In: *MNRAS* 481.4, pp. 4984–4999. DOI: 10.1093/mnras/sty2607. arXiv: 1809.07965 [astro-ph.SR].

Mellema (Oct. 1994). "The gasdynamic evolution of spherical planetary nebulae. Radiation-gasdynamics of PNe III." In: *A&A* 290, pp. 915–935. arXiv: astro-ph/9405048 [astro-ph].

Mellema, Eulderink, and Icke (Dec. 1991). "Hydrodynamical models of aspherical planetary nebulae". In: *A&A* 252, pp. 718–732.

Miller Bertolami (Apr. 2016). "New models for the evolution of post-asymptotic giant branch stars and central stars of planetary nebulae". In: *A&A* 588, A25, A25. DOI: 10.1051/0004-6361/201526577. arXiv: 1512.04129 [astro-ph.SR].

Mohamed and Podsiadlowski (Sept. 2007). "Wind Roche-Lobe Overflow: a New Mass-Transfer Mode for Wide Binaries". In: *15th European Workshop on White Dwarfs*. Ed. by R. Napiwotzki and M.R. Burleigh. Vol. 372. Astronomical Society of the Pacific Conference Series, p. 397.

Nordhaus, Blackman, and Frank (Apr. 2007). "Isolated versus common envelope dynamos in planetary nebula progenitors". In: *MNRAS* 376.2, pp. 599–608. DOI: 10.1111/j.1365-2966.2007.11417.x. arXiv: astro-ph/0609726 [astro-ph].

Norris et al. (Apr. 2012). "A close halo of large transparent grains around extreme red giant stars". In: *Nature* 484.7393, pp. 220–222. DOI: 10.1038/nature10935. arXiv: 1204.2640 [astro-ph.SR].

Nowotny, Höfner, and Aringer (May 2010). "Line formation in AGB atmospheres including velocity effects. Molecular line profile variations of long period variables". In: *A&A* 514, A35, A35. DOI: 10.1051/0004-6361/200911899. arXiv: 1002.1849 [astro-ph.SR].

Ohlmann et al. (Jan. 2016). "Hydrodynamic Moving-mesh Simulations of the Common Envelope Phase in Binary Stellar Systems". In: *ApJ* 816, L9, p. L9. DOI: 10.3847/2041-8205/816/1/L9. arXiv: 1512.04529 [astro-ph.SR].

Ostlie and Cox (Dec. 1986). "A linear survey of the Mira variable star instability region of the Hertzsprung-Russell diagram". In: *ApJ* 311, pp. 864–872. DOI: 10.1086/164824.

Paczynski (Sept. 1977). "A model of accretion disks in close binaries." In: *ApJ* 216, pp. 822–826. DOI: 10.1086/155526.

Paczyński (Jan. 1965). "Cataclysmic Variables among Binary Stars I. U Geminorum Stars". In: *Acta Astron.* 15, p. 89.

— (1971). "Evolutionary Processes in Close Binary Systems". In: *ARA&A* 9, p. 183. DOI: 10.1146/annurev.aa.09.090171.001151.

Paczyński and Ziółkowski (Jan. 1968). "On the Origin of Planetary Nebulae and Mira Variables". In: *Acta Astron.* 18, p. 255.

Parker et al. (Nov. 2006). "The Macquarie/AAO/Strasbourg Hα Planetary Nebula Catalogue: MASH". In: *MNRAS* 373.1, pp. 79–94. DOI: 10.1111/j.1365-2966.2006.10950.x.

Passy et al. (Jan. 2012). "Simulating the Common Envelope Phase of a Red Giant Using Smoothed-particle Hydrodynamics and Uniform-grid Codes". In: *ApJ* 744, 52, p. 52. DOI: 10.1088/0004-637X/744/1/52. arXiv: 1107.5072 [astro-ph.SR].

Pauldrach et al. (Dec. 1988). "Radiation-driven winds of hot stars. V. Wind models for central starsof planetary nebulae." In: *A&A* 207, pp. 123–131.

Pavlovskii and Ivanova (June 2015). "Mass transfer from giant donors". In: *MNRAS* 449.4, pp. 4415–4427. DOI: 10.1093/mnras/stv619. arXiv: 1410.5109 [astro-ph.SR].

Pejcha, Metzger, and Tomida (Feb. 2016). "Cool and luminous transients from mass-losing binary stars". In: *MNRAS* 455, pp. 4351–4372. DOI: 10.1093/mnras/stv2592. arXiv: 1509.02531 [astro-ph.SR].

Perinotto, M. et al. (Feb. 2004). "The evolution of planetary nebulae. I. A radiation-hydrodynamics parameter study". In: *A&A* 414, pp. 993–1015. DOI: 10.1051/0004-6361:20031653.

Prust and Chang (July 2019). "Common envelope evolution on a moving mesh". In: *MNRAS* 486.4, pp. 5809–5818. DOI: 10.1093/mnras/stz1219. arXiv: 1904.09256 [astro-ph.SR].

Ramstedt, Schöier, and Olofsson (May 2009). "Circumstellar molecular line emission from S-type AGB stars: mass-loss rates and SiO abundances". In: *A&A* 499.2, pp. 515–527. DOI: 10.1051/0004-6361/200911730. arXiv: 0903.1672 [astro-ph.SR].

Randall et al. (Apr. 2020). "Discovery of a complex spiral-shell structure around the oxygen-rich AGB star GX Monocerotis". In: *A&A* 636, A123, A123.

Rau, Nielsen, et al. (Dec. 2018). "HST/GHRS Observations of Cool, Low-gravity Stars. VI. Mass-loss Rates and Wind Parameters for M Giants". In: *ApJ* 869.1, 1, p. 1. DOI: 10.3847/1538-4357/aaf0a0. arXiv: 1811.10679 [astro-ph.SR].

Rau, Paladini, et al. (Nov. 2015). "Modelling the atmosphere of the carbon-rich Mira RU Virginis". In: *A&A* 583, A106, A106. DOI: 10.1051/0004-6361/201526418. arXiv: 1506.03978 [astro-ph.SR].

Reichardt et al. (Mar. 2019). "Extending common envelope simulations from Roche lobe overflow to the nebular phase". In: *MNRAS* 484.1, pp. 631–647. DOI: 10.1093/mnras/sty3485. arXiv: 1809.02297 [astro-ph.SR].

Renzini (1981). "Red giants as precursors of planetary nebulae". In: *Physical Processes in Red Giants*. Ed. by I. Iben Jr. and A. Renzini. Vol. 88. Astrophysics and Space Science Library, pp. 431–446. DOI: 10.1007/978-94-009-8492-9_48.

Ricker and Taam (Feb. 2012). "An AMR Study of the Common-envelope Phase of Binary Evolution". In: *ApJ* 746, 74, p. 74. DOI: 10.1088/0004-637X/746/1/74. arXiv: 1107.3889 [astro-ph.SR].

Ruffert (Dec. 1993). "Collisions between a white dwarf and a main-sequence star. 3: Simulations including the white dwarf surface". In: *A&A* 280, pp. 141–156.

Sabach et al. (Dec. 2017). "Energy transport by convection in the common envelope evolution". In: *MNRAS* 472.4, pp. 4361–4367. DOI: 10.1093/mnras/stx2272. arXiv: 1706.05838 [astro-ph.SR].

Sahai et al. (Dec. 2007). "Preplanetary Nebulae: A Hubble Space Telescope Imaging Survey and a New Morphological Classification System". In: *AJ* 134.6, pp. 2200–2225. DOI: 10.1086/522944. arXiv: 0707.4662 [astro-ph].

Sana et al. (July 2012). "Binary Interaction Dominates the Evolution of Massive Stars". In: *Science* 337.6093, p. 444. DOI: 10.1126/science.1223344. arXiv: 1207.6397 [astro-ph.SR].

Schwarz and Monteiro (July 2004). "Binarity and Symbiotics in Asymmetrical Planetary Nebulae". In: *Asymmetrical Planetary Nebulae III: Winds, Structure and the Thunderbird*. Ed. by M. Meixner et al. Vol. 313. Astronomical Society of the Pacific Conference Series, p. 497. eprint: astro-ph/0310074.

Sepinsky et al. (Sept. 2009). "Interacting Binaries with Eccentric Orbits. II. Secular Orbital Evolution due to Non-conservative Mass Transfer". In: *ApJ* 702.2, pp. 1387–1392. DOI: 10.1088/0004-637X/702/2/1387. arXiv: 0903.0621 [astro-ph.SR].

Shiber et al. (Oct. 2019). "Companion-launched jets and their effect on the dynamics of common envelope interaction simulations". In: *MNRAS* 488, pp. 5615–5632. DOI: 10.1093/mnras/stz2013. arXiv: 1902.03931 [astro-ph.SR].

Shu, Lubow, and Anderson (Apr. 1979). "On the structure of contact binaries. III - Mass and energy flow". In: *ApJ* 229, pp. 223–241. DOI: 10.1086/156948.

Sloan et al. (Aug. 2010). "Spitzer Spectroscopy of Mass-loss and Dust Production by Evolved Stars in Globular Clusters". In: *ApJ* 719.2, pp. 1274–1292. DOI: 10.1088/0004-637X/719/2/1274. arXiv: 1006.5016 [astro-ph.GA].

Soker (Apr. 2002). "Formation of Bipolar Lobes by Jets". In: *ApJ* 568.2, pp. 726–732. DOI: 10.1086/339065.

Soker and Livio (Apr. 1989). "Interacting winds and the shaping of planetary nebulae". In: *ApJ* 339, pp. 268–278. DOI: 10.1086/167294.

Staff et al. (Feb. 2016). "Hydrodynamic simulations of the interaction between an AGB star and a main-sequence companion in eccentric orbits". In: *MNRAS* 455, pp. 3511–3525. DOI: 10.1093/mnras/stv2548. arXiv: 1510.08429 [astro-ph.SR].

Stanghellini et al. (Nov. 2006). "Planetary Nebula Abundances and Morphology: Probing the Chemical Evolution of the Milky Way". In: *ApJ* 651, pp. 898–905. DOI: 10.1086/507840. eprint: astro-ph/0607480.

Sweby (Oct. 1984). "High Resolution Schemes Using Flux Limiters for Hyperbolic Conservation Laws". In: *SIAM Journal on Numerical Analysis* 21.5, pp. 995–1011. DOI: 10.1137/0721062.

Toledo-Roy et al. (Jan. 2014). "A blowout numerical model for the supernova remnant G352.7-0.1". In: *MNRAS* 437, pp. 898–905. DOI: 10.1093/mnras/stt1955.

Toro (June 2019). "The HLLC Riemann solver". In: *Shock Waves* 29.8, pp. 1065–1082. DOI: 10.1007/s00193-019-00912-4.

Toro, Spruce, and Speares (July 1994). "Restoration of the contact surface in the HLL-Riemann solver". In: *Shock Waves* 4.1, pp. 25–34. DOI: 10.1007/BF01414629.

Torres, Andersen, and Giménez (Feb. 2010). "Accurate masses and radii of normal stars: modern results and applications". In: *A&ARv* 18.1-2, pp. 67–126. DOI: 10.1007/s00159-009-0025-1. arXiv: 0908.2624 [astro-ph.SR].

Townsend (Apr. 2009). "An Exact Integration Scheme for Radiative Cooling in Hydrodynamical Simulations". In: *ApJS* 181, pp. 391–397. DOI: 10.1088/0067-0049/181/2/391. arXiv: 0901.3146 [astro-ph.SR].

Tuchman, Sack, and Barkat (Jan. 1978). "Mass loss from dynamically unstable stellar envelopes." In: *ApJ* 219, pp. 183–194. DOI: 10.1086/155767.

Vaidya et al. (Aug. 2015). "Astrophysical fluid simulations of thermally ideal gases with non-constant adiabatic index: numerical implementation". In: *A&A* 580, A110, A110. DOI: 10.1051/0004-6361/201526247. arXiv: 1506.01562 [astro-ph.IM].

van Belle, Thompson, and Creech-Eakman (Sept. 2002). "Angular Size Measurements of Mira Variable Stars at 2.2 Microns. II." In: *AJ* 124.3, pp. 1706–1715. DOI: 10.1086/342282. arXiv: astro-ph/0210167 [astro-ph].

Van Winckel et al. (Jan. 2006). "Binary post-AGB stars and their Keplerian discs ." In: *Mem. Soc. Astron. Italiana* 77, p. 943. arXiv: astro-ph/0604172 [astro-ph].

Vassiliadis and Wood (Aug. 1993). "Evolution of low- and intermediate-mass stars to the end of the asymptotic giant branch with mass loss". In: *ApJ* 413, pp. 641–657. DOI: 10.1086/173033.

Whitelock, Patricia A., Michael W. Feast, and Floor Van Leeuwen (May 2008). "AGB variables and the Mira period-luminosity relation". In: *MNRAS* 386.1, pp. 313–323. DOI: 10.1111/j.1365-2966.2008.13032.x. arXiv: 0801.4465 [astro-ph].

Williams and Cieza (Sept. 2011). "Protoplanetary Disks and Their Evolution". In: *ARA&A* 49.1, pp. 67–117. DOI: 10.1146/annurev-astro-081710-102548. arXiv: 1103.0556 [astro-ph.GA].

Wittkowski et al. (June 2018). "VLTI-GRAVITY measurements of cool evolved stars. I. Variable photosphere and extended atmosphere of the Mira star R Peg". In: *A&A* 613, L7, p. L7. DOI: 10.1051/0004-6361/201833029. arXiv: 1805.05333 [astro-ph.SR].

Woitke, Krueger, and Sedlmayr (July 1996). "On the gas temperature in the shocked circumstellar envelopes of pulsating stars. I. Radiative heating and cooling rates." In: *A&A* 311, pp. 927–944.

Wood (Jan. 1979). "Pulsation and mass loss in Mira variables." In: *ApJ* 227, pp. 220–231. DOI: 10.1086/156721.

— (Apr. 2000). "Variable Red Giants in the LMC: Pulsating Stars and Binaries?" In: *Publ. Astron. Soc. Australia* 17.1, pp. 18–21. DOI: 10.1071/AS00018.

Zahn (May 1977). "Reprint of 1977A&A....57..383Z. Tidal friction in close binary stars." In: *A&A* 500, pp. 121–132.